Macalester Journal of Physics and Astronomy

Volume 12
Issue 1 *Spring 2024*

Article 3

May 2024

Variability of High-Degree Modes over Multiple Solar Cycles Using Local Helioseismic Data from GONG

Nicholas Cebula
Macalester College, ncebula@macalester.edu

Sushanta Tripathy
National Solar Observatory, stripathy@nso.edu

Kiran Jain
National Solar Observatory, kjain@nso.edu

John M. Cannon
Macalester College, jcannon@macalester.edu

Variability of High-Degree Modes over Multiple Solar Cycles Using Local Helioseismic Data from GONG

Abstract

In this investigation we use the local helioseismic technique of ring diagrams to study the power, energy, and damping rates of high degree solar acoustic modes. Our data covers the period from the maximum phase of solar cycle 23 to the ascending phase of cycle 25. The goal is to examine the variations in the mode parameters with solar activity as well as the differences between different cycles. For this, we use different proxies of solar activity. We use 10.7 cm radio flux measurements and a measure of magnetic flux known as magnetic activity index from magnetograms.

Keywords

helioseismology, physics, solar physics, python

MACALESTER COLLEGE

Variability of High-Degree Modes over Multiple Solar Cycles Using Local Helioseismic Data from GONG

by

Nicholas Cebula

in the

Department of Physics and Astronomy

Advisors: Sushanta Tripathy, Kiran Jain, John Cannon

April 2024

MACALESTER COLLEGE

Abstract

Department of Physics and Astronomy

by Nicholas Cebula

In this investigation we use the local helioseismic technique of ring diagrams to study the power, energy and damping rates of high degree solar acoustic modes. Our data is derived from Doppler observations of the Global Oscillations Network Group (GONG) and covers the period 2001-2022 i.e. from the maximum phase of solar cycle 23 to the ascending phase of cycle 25. The goal is to examine the variations in the mode parameters, e.g., mode amplitude, life time of the modes, and energy associated with the modes with solar activity as well as the differences and similarities between different cycles since each solar cycle behaves differently. For this, we use different proxies of solar activity. In particular, we use 10.7 cm radio flux measurements and a local measure of magnetic flux known as magnetic activity index calculated from magnetograms. We find a strong positive correlation between magnetic flux and mode width which is proportional to the damping rate. Thus we find that the modes are maximally damped during the period of maximum solar activity. We further find that the mode amplitude is in anti-phase with magnetic flux, where amplitude values are found to be decreasing during periods of high magnetic flux. This relation holds true for the majority of the years analyzed here. However, there are a few anomalous periods of time where the amplitude values appear to be in phase with magnetic flux. While the exact reason for this has not yet been found, we cannot rule out an instrumental origin.

Acknowledgements

I would like to offer thanks to the Boulder Solar Alliance for providing the REU opportunity and the National Solar Observatory. This work utilises GONG data obtained by the NSO Integrated Synoptic Program, managed by the National Solar Observatory, which is operated by the Association of Universities for Research in Astronomy (AURA), Inc. under a cooperative agreement with the National Science Foundation and with contribution from the National Oceanic and Atmospheric Administration. The GONG network of instruments is hosted by the Big Bear Solar Observatory, High Altitude Observatory, Learmonth Solar Observatory, Udaipur Solar Observatory, Instituto de Astrofísica de Canarias, and Cerro Tololo Interamerican Observatory. I would also like to thank my family, friends, and the Macalester Physics and Astronomy department for all the support and guidance they have offered me.

Contents

List of Figures

List of Tables

CHAPTER 1: Introduction

1.1 Helioseismology

The scientific field of helioseismology is a relatively new one, having began in the 1970s after the discovery of propagating sound waves in the Sun in the 1960s (Leighton et al. 1962). Up until this point, the knowledge of the Sun's interior was theoretical, as the regions of the Sun below its surface (the photosphere) can not be observed directly. Once propagating sound waves similar to Earth's seismic waves were discovered in the Sun, the ability to indirectly explore regions below the photosphere became available to solar physicists (Leibacher et al. 1985). Just as geophysicists observe Earth's seismic waves to learn about the interior of the Earth, helioseismologists observe the oscillating waves as they appear on the surface of the Sun to learn about the solar interior.

There are two main categories of the oscillating modes of vibration in the solar interior: acoustic and gravity waves. Pressure is the restoring force for acoustic waves (p-modes) while buoyancy is the restoring force for internal gravity waves (g-modes), similar to a buoyant object bouncing up and down on a water surface (Leibacher et al. 1985). There does exist what are referred to as surface gravity modes, or f-modes, which have a buoyant restoring force but occur on the surface of the Sun. Gravity waves originate closer to the core of the Sun and the radiative zone. This makes gravity waves highly valuable for learning about the core of the Sun. However, gravity waves are unable to be detected as they can not travel through the Sun's convective layer. This has made acoustic waves the main area of focus for helioseismologists, and thus the focus of this research. Different layers of solar interior and the atmosphere are shown in Figure 1.1.

The p-modes are able to propagate throughout the solar interior due to the Sun acting as a large resonant cavity. These waves undergo reflection when certain conditions are satisfied and hence carry information from depths where they are confined. High-degree p-modes are confined very close to the surface and hence carry information from those layers. When acoustic waves reach the surface of the

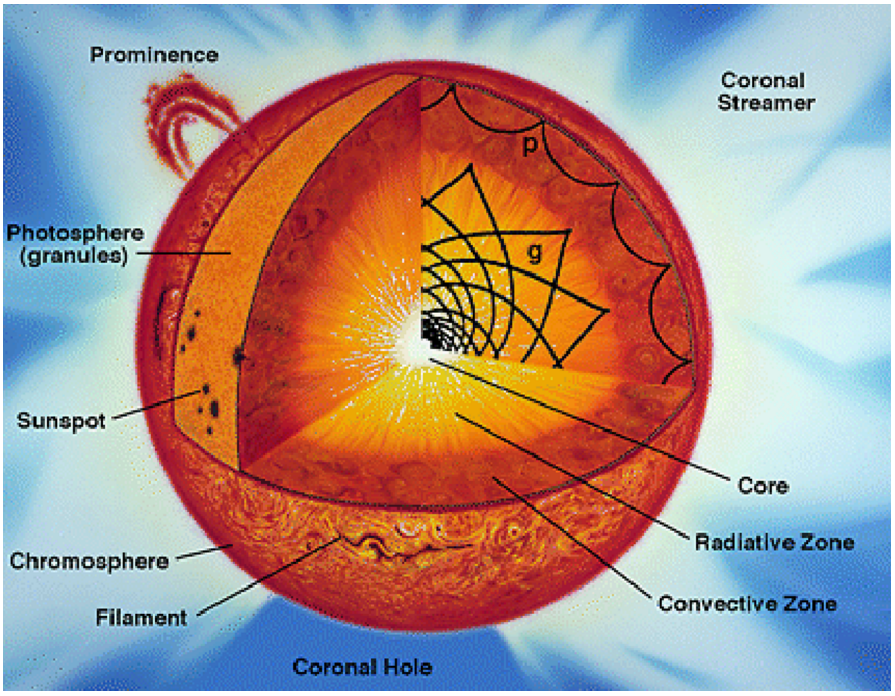

FIGURE 1.1: An illustrated example showing the solar atmosphere, interior and example paths of p- and g-modes in the Sun. Due to the increase of the speed of sound with depth, the deeper parts of the wave fronts move faster. Waves with a smaller wavelength, corresponding to a higher value of the degree ℓ, penetrate less deeply.

Sun, they cause the gases there to move up and down. This results in shifting wavelengths of the spectral lines which are measured by observing the Doppler shifts of the spectral lines (see Figure 1.2). This movement also changes the temperature of the gas, and therefore changes the brightness of the gas, meaning acoustic modes can be detected through observation of small fluctuations in the brightness of the Sun's surface.

Over the past few decades there has been an abundance of both space-based and ground-based observations of acoustic modes of vibration. The space based data initially came from the Michelson Doppler Imager (MDI) onboard solar and heliospheric Observatory (SoHO) until its termination in 2011, and now more modern data comes from the Helioseismic and Magnetic Imager (HMI) onboard the solar Dynamics Observatory (SDO) (which is positioned at inclined geosynchronous circular orbit). Ground-based data comes from the Global Oscillations Network Group (GONG), a network of six telescopes spread across the globe, shown in

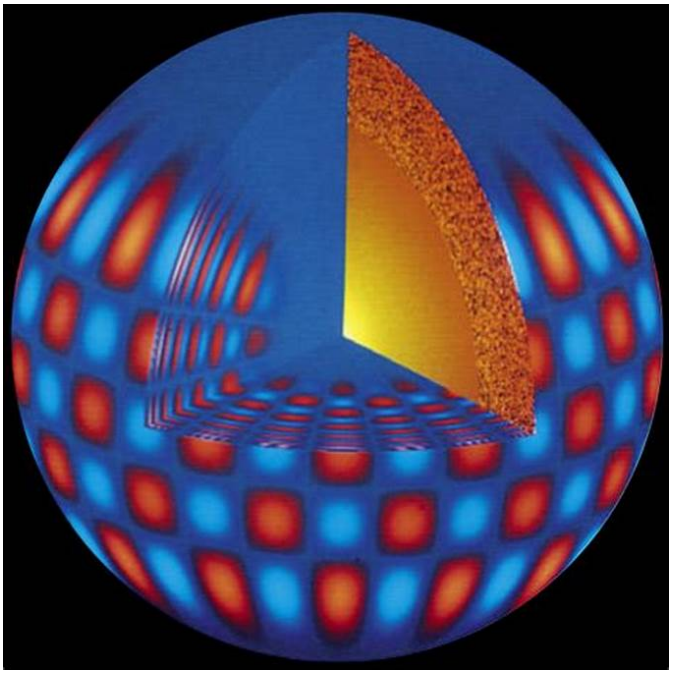

FIGURE 1.2: Schematic diagram of acoustic modes showing regions of approaching (blue) and receding (red) velocities on both surface and the interior of the Sun. These velocity shifts are due to gas displacement from the acoustic modes.

Figure 1.3, to achieve uninterrupted observation of the Sun when each location's data is pooled together (Jain et al. 2021). The relevant data for this project is gathered from GONG, and the results are exclusively from ground-based data.

One use of the data from both GONG and SDO has been to study the changes in various parameters of acoustic modes, such as excitation (generation of the mode) and damping (dissipation of the energy of a mode). The changes in the parameters of these acoustic modes are believed to be caused by a variable magnetic field generated by a dynamo and therefore the changes potentially can tell us about the internal properties of the Sun (Howe et al. 2004).

The global acoustic modes that are detected on the Sun's surface can be modeled as spherical harmonics and thus distinctly recognized due to three primary wave numbers; n, ℓ, and m. The wave number n refers to the radial order of the wave, or the number of nodes per unit distance, azimuthal order m is the number of nodal lines around the equator. The spherical harmonic degree ℓ is the total number of nodal lines on the solar surface or the number of nodes along a great circle at

FIGURE 1.3: A layout of the six locations of the GONG observatories. The spread of the observatories means that even if one of the sites is down for construction/maintenance, the Sun will still be observed the entirety of the day by neighboring sites. Figure from Jain et al. (2021).

an angle to the equator. However, considering plane wave description, which is relevant to our analysis, the modes are considered to be local waves that are not affected by the spherical shape of the Sun. In this representation the wave number ℓ is calculated with the equation:

$$\ell = k \cdot R_{\odot} \tag{1.1}$$

where k is horizontal wave number and $R_{\odot}$ is the solar radius. The range of n and ℓ data for this research range from 0-6 and 180-1300, although some modes of n values 5/6 and higher ℓ values are neglected in this analysis as the data on such modes has higher errors. These individual modes can be seen visually when the frequency of the acoustic modes is plotted vs their ℓ degree, as seen in Figure 1.4.

1.2 Motivation

Earlier studies involving low-degree modes ($\ell \leq 4$) found inverse correlation between the amplitude (excitation) of modes with the solar activity level and a direct

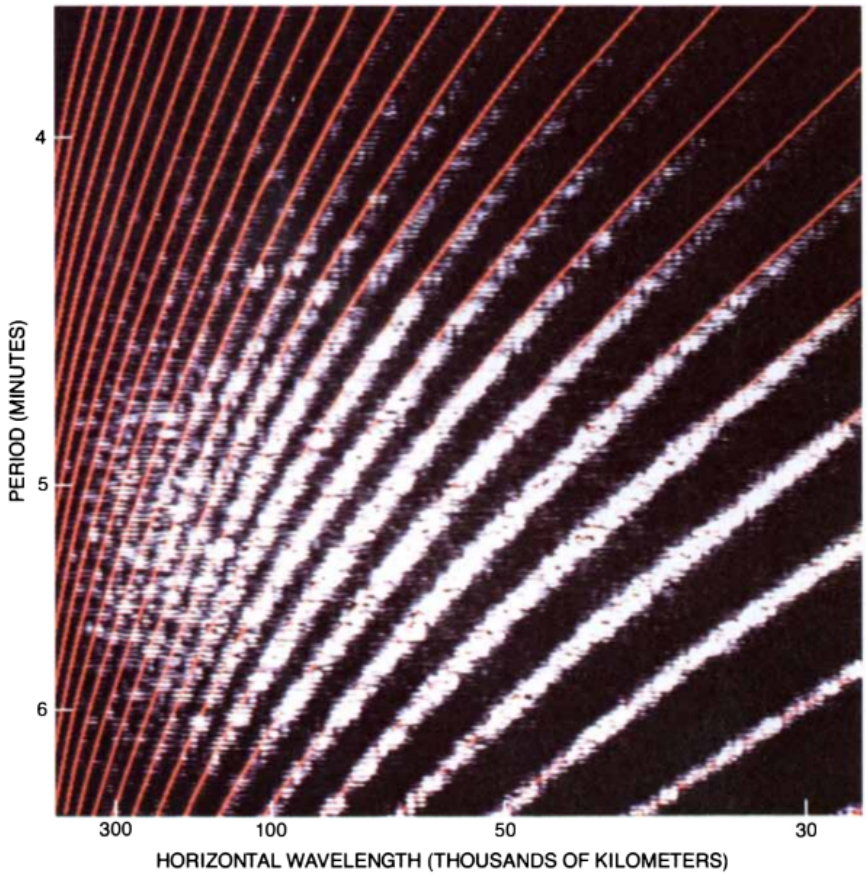

FIGURE 1.4: A visual demonstration of how the resonant acoustic modes of the solar interior are observed at the surface. Only waves with specific combinations of period and horizontal wave-length should resonate within the Sun. The colored curves indicate theoretical predictions for resonant modes, based on a standard solar model while the bright ridges are from observations. Figure from Leibacher et al. (1985).

correlation between the mode width (damping) and solar activity level (Chaplin et al. 2004; Elsworth et al. 1993). Based on the magnitude of the change, it was suggested that the changes primarily arise from changes to the damping of a mode rather than a change to the mode's excitation. Komm et al. (2000a,b) also found similar changes in the amplitude and width of medium-degree modes ($4 \leq \ell \leq 300$) using data from GONG. With the availability of high-resolution Dopplergrams (a two-dimensional image of the approaching and receding velocities of the Sun, Figure 1.5), Howe et al. (2004) used the ring-diagram technique (defined in chapter 2) of local helioseismology to investigate the amplitude and mode width of high-degree solar oscillations and found that the mode parameters show a strong

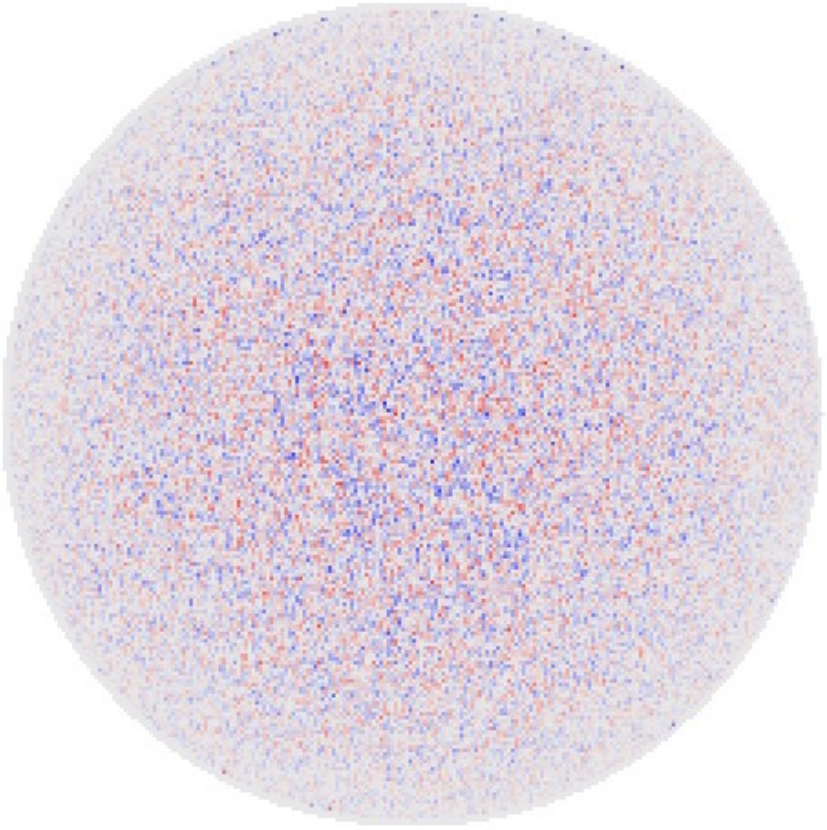

FIGURE 1.5: An example Dopplergram showing the solar oscillations. Here the red and blue color denotes redshifted and blueshifted velocities of plasma on the solar disk.

dependence on the local magnetic activity. These authors also found that mode amplitude and mode lifetime (which is the inverse of the mode width) decrease at high frequencies with respect to magnetic activity.

Recent studies involving low-degree modes from the Birmingham solar Oscillations Network (BiSON) incorporating data over a few solar cycles confirmed previous results that at solar activity maximum the oscillations are most heavily damped (mode widths are maximum) and the mode powers/excitation are at a minimum (mode amplitudes are minimum) (Broomhall et al. 2015). BiSON is a global network of six ground based telescopes providing constant monitoring of the Sun for the study of its oscillation modes, similar to GONG. Regressing the solar activity through the proxy of 10.7 cm radio flux (F10.7 hereafter) the authors found a good agreement between the damping rates and radio flux but noted

deviations in the mode amplitude during solar cycle 22 and 24. I further detail what the radio flux parameter is and how it is obtained in the data analysis chapter of this paper. This implies that the relation between mode powers and solar activity is not consistent from one cycle to another, but rather changes each solar cycle. They also inferred that the energy supply rate, or the rate of change of an oscillation's energy, to be decreasing with time when it had previously been observed as constant with solar cycle. The analysis of these parameters using GONG global p-mode data over two solar cycles (Kiefer & Broomhall 2021) further confirmed that the energy supply rates are anti-correlated with the level of solar activity, for which F10.7 index was again used as a proxy. These results suggest that energy supply rate, once thought to be constant with time, is in fact changing with respect to solar activity.

Since it has been demonstrated that the relation between low and intermediate degree mode parameters and solar activity changes between solar cycles (Figure 4.6), we have endeavoured to study the changes in these parameters over multiple solar cycles, starting from the maximum phase of solar cycle 23 to the ascending phase of cycle 25 using the high-degree modes computed by GONG since July 2001.

CHAPTER 2: Data Sources & Processing

The data for this project comes from six ground based GONG observatories distributed around the globe to allow for continuous collection of data of the Sun regardless of day/night cycle (Figure 1.3). The high-degree mode frequencies used in this study are computed from GONG 1-minute cadence full-disk Dopplergrams that are computed with the merged data from each GONG site (Harvey et al. 1998, 1996) (example in Figure 1.5) and cover the period from June 26, 2001 to December 09, 2022. This time range includes approximately the last seven years of cycle 23, all of cycle 24, and the first year and a half of cycle 25. Each GONG site receives around 6-8 hours of data individually each day, and these are combined to produce continuous merged Dopplergrams without affecting the diurnal cycles at sites. I discuss below how these Dopplergrams are used in my study of local helioseismology of the Sun.

While global helioseismology uses the entire disk of the Sun as a single entity, local helioseismology splits the Sun into a series of small regions or patches, and performs data analysis on these separate pieces of the Sun's disk (Hill 1988). These individual patches are squares of size 15° of longitude and 15° of latitude, and overlap with four other patches in each of their corners by 7.5°. The patches are made on a cylindrical projection of equal arc length of the Sun's disk. This ensures that all of the patches regardless of longitude and latitude are of equal area. Since the patches closer to the solar limb are not well resolved, we neglect the patches which are located higher than ± 52.5° in latitude and longitudinal directions and thus analyze only 189 patches (Corbard et al. 2003). In order to remove solar rotation, Dopplergrams are tracked by a known differential rotation rate for 1664 minutes; 1664 minutes is the amount of time it takes the Sun to rotate by 15°, meaning that a patch on a GONG day at 0° longitude (the central meridian) will be at 15° west longitude the following day.

The acoustic mode parameters are computed using Dopplergrams processed through the standard GONG ring-diagram pipeline (Corbard et al. 2003; Hill et al. 2003) which creates a three-dimensional spectra with two dimensions in space and one in time of a given region on the surface of the Sun. A good and in-depth description

of the ring-diagram technique can be found in (Hill 1988) but for sake of completeness we present a brief outline of the procedure used in this work (see Figure 2.1). The solar surface in each Dopplergram is divided into 189 overlapping regions (or patches) covering $\pm 52.5^\circ$ in latitude and central meridian distance, spaced by 7.5° in either direction. Each patch covers an area of $15^\circ \times 15^\circ$ in heliographic longitude and latitude, and is tracked for 1664 minutes (hereafter 'ring-day') using the solar rotation rate (Snodgrass 1984).

Finally, each patch is passed through a 3-dimensional fast Fourier transform (FFT). The FFT is done to each of the 189 patches. Since this FFT is a 3D Fourier transform, the Dopplergram data with axes of x, y and time are converted from time space to frequency space, with x and y becoming wave numbers k_x and k_y. After the FFT, the shape of the data takes on a trumpet morphology (Figure 2.2), and taking individual slices of this trumpet at a constant frequency will produce a two dimensional graph (k_x and k_y) with a series of rings morphology that the technique's name is derived from (see Figure 2.1). To derive different mode parameters 3D power spectra are fitted with a Lorentzian profile described by the following equation (Haber et al. 2000):

$$P\left(k_x, k_y, \nu\right) = \frac{A\Gamma/2}{\left(\omega - \omega_0 + k_x U_x + k_y U_y\right)^2 + (\Gamma/2)^2} + \frac{b_0}{k^3} \tag{2.1}$$

where P is the oscillation power for a wave with a temporal frequency ν and a wave number k ($k^2 = \sqrt{(k_x^2 + k_y^2)}$. U_x, U_y, ν, Γ, b_0 and A are parameters that need to be fitted. U_x and U_y are the zonal and meridional velocities, respectively, ν is the central frequency, A is the amplitude, Γ is the mode width, and b_0 is the background power. The fitting procedure provides about 200 modes that have ℓ values between 180 and 1300 in the frequency range from 1700 μHz to 5600 μHz.

GONG is a ground-based instrument and experiences gaps in observations due to weather conditions and maintenance of instruments (Jain et al. 2021). We define duty cycle as the percentage of good observations out of 1664 minutes, and since the mode parameters corresponding to low duty cycle have large errors (e.g., Keith-Hardy et al. 2019), we exclude the data if the duty cycle is less than 70%.

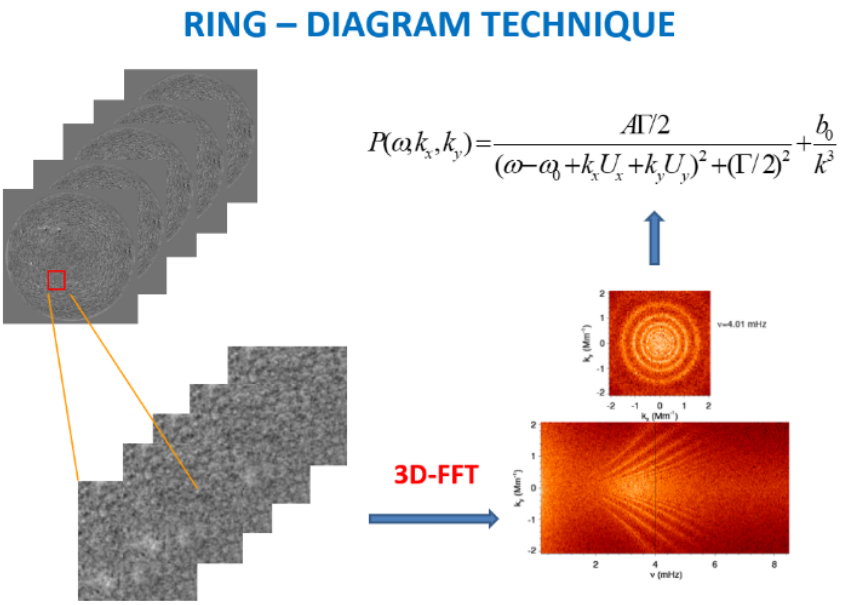

FIGURE 2.1: A visual example of the ring diagram technique, with patches going through a 3D FFT for each of the 1664 Dopplergrams. A Lorentzian profile is applied to the power spectra to get mode parameters as described in the equation.

2.1 Corrections for duty cycle and center-to-limb variation

As mentioned above, the mode parameters measured by the ring-diagram technique are affected by foreshortening as well as gaps in observation (Jain et al. 2013, 2021). Although we exclude days with a duty cycle less than 70% in this study, we further correct all mode parameters for duty cycle variation as well as for geometric variation. The duty cycle corrections are done since each ring day has a different value (Figure 2.3). The geometric correction is required since the solar disk is not equally resolved at the disk center and the solar limb. This issue is also amplified by the amount of solar atmosphere that one must look through when looking at the edge patches of the Sun is much larger than the straight path of looking at the Sun's center. As a result, the ring diagram power spectra suffer from the effect of projection as shown in Figure 2.4. The in-homogeneity in rings is clearly visible in the mosaic shown in this figure. Following the method outlined

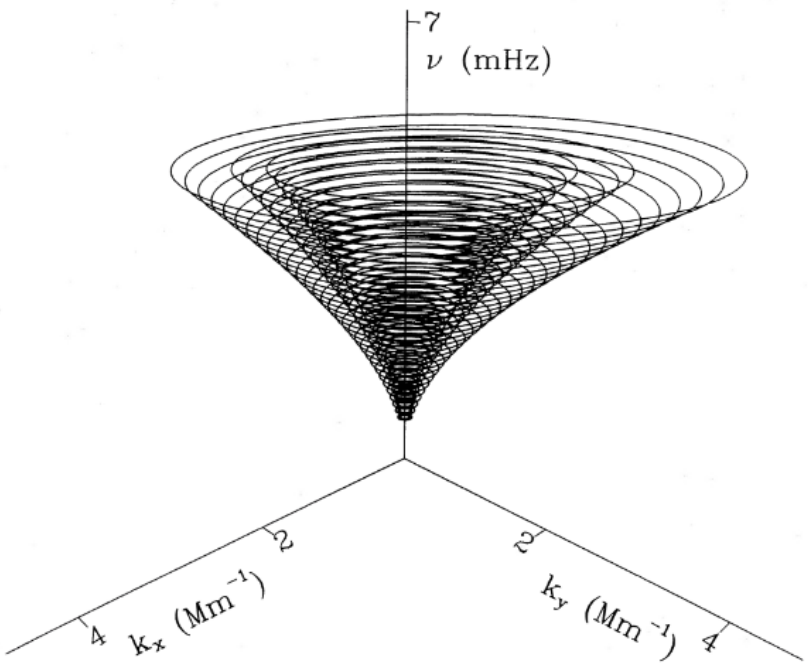

FIGURE 2.2: A depiction of the trumpet morphology that is produced by applying a 3D FFT to a patch. Figure from (Hill 1988). The three axes are horizontal and vertical wave number and frequency.

by Howe et al. (2004), we model the effects of position of the solar disk as a two-dimensional function of the distance from disk center ρ without the cross-terms, combined with a linear dependence on the fill factor, $f(t)$,

$$C(\rho_x, \rho_y, t) = a_0 + a_1\rho_x + a_2\rho_x^2 + a_3\rho_y + a_4\rho_y^2 + a_5 f(t), \tag{2.2}$$

where C is the mode parameter (excitation, damping rate, etc.), ρ_x and ρ_y are the longitude and latitude coordinates of the center of the patch, and the a_i's are coefficients determined by fitting.

While the data reduction techniques for local helioseismology are outlined and described in this section, these procedures were not something personally performed for this research. Rather, the data was at a point where the ring-diagram technique and corrections were already fully applied to the dataset. This left the starting point for this project at the averaging and analysis of the mode parameters, whose data valued were fully calculated. This meant the data was sorted so that there were 189 files, one per patch, for each day of the data range spanning from July

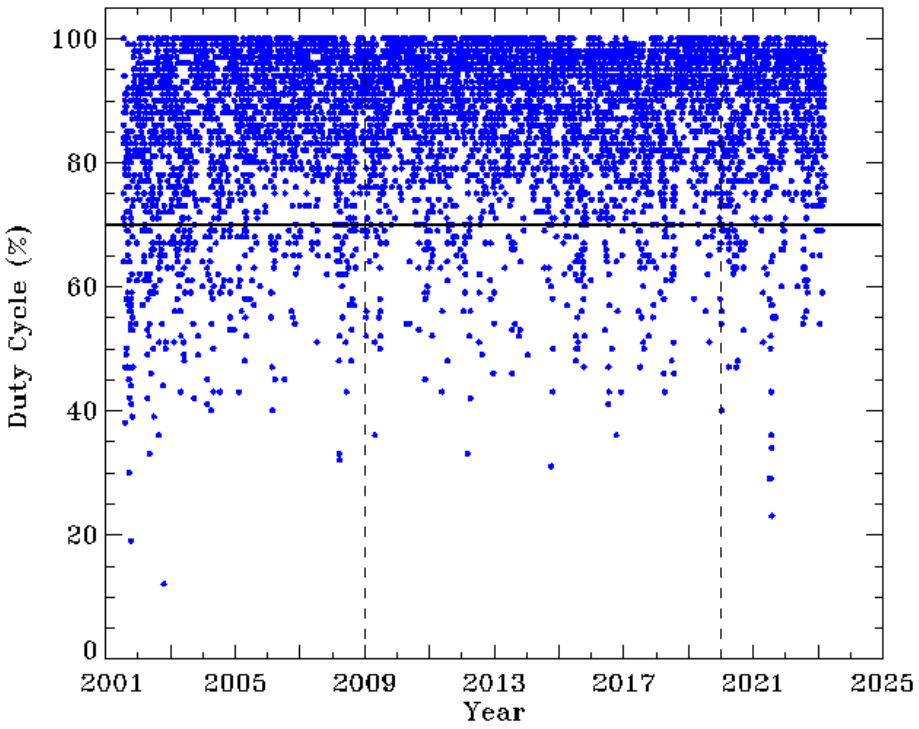

FIGURE 2.3: GONG duty cycle as a function of time. The solid black horizontal line shows the threshold of 70%. Days with duty cycle values below this threshold were not used as the determined mode parameters tend to have large uncertainty.

2001 to **December** 2022. Each individual file had multiple amplitude and mode width parameter values, each of different n and ℓ, as well as longitudinal and latitudinal coordinates and a date. This totaled to a raw number of around 1.4 million files, and this research revolved mainly around analyzing this large number of files to find the changes in excitation and damping rates with different solar activity cycles.

2.2 Measures of solar Activity

Since mode parameters are known to vary with solar activity cycle, we compute a quantity known as "magnetic activity index" (MAI) as a measure of solar activity. For each tile, a data cube is generated by tracking and re-mapping line-of-sight

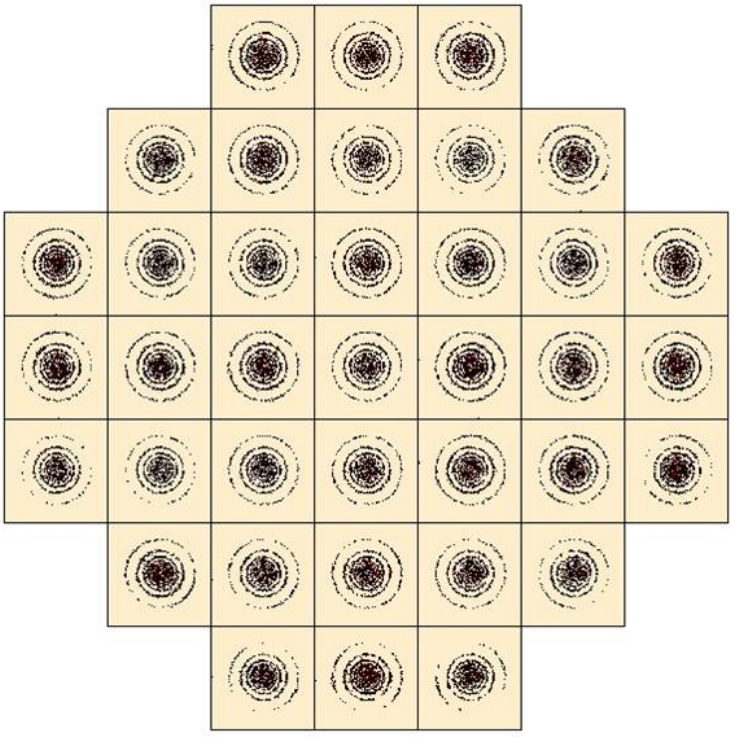

FIGURE 2.4: Mosaic showing the effect of projection of the ring diagram technique applied to multiple patches, with the patch in the center of the image being the disk center patch. The other patches are the ring diagram technique on the neighboring patches of the disk center, with the further away a patch is equating to the patch being further in longitude/latitude. These rings represent the cuts in power spectra at a fixed frequency. The patch at the center corresponds to the disk center. Here the resolution and geometric issues can be seen, where the rings in the outer patches are not as complete as patches towards the center.

magnetograms in the same fashion as Dopplergrams. A magnetogram is an image that shows the strength, polarity, and location of the magnetic fields on the surface of the Sun. The absolute values of each pixel higher than a specified threshold in the data cube are then averaged to compute the MAI. It may be noted that the merged GONG magnetograms are not available for 2001–2007, hence we use 96-minute magnetograms from the Michelson Doppler Imager (MDI) up to 2007 April 9 and GONG magnetograms sampled every 32 minutes thereafter[1]. The threshold value for MDI magnetograms is set to 50 G (Basu et al. 2004) and 8.8 G for GONG data which are approximately 2.5 times the estimated noise in

[1] https://gong2.nso.edu/ftp/oDM/bzi/

individual magnetograms. To generate uniform MAI values over the entire period, MDI values are scaled to the GONG values by a conversion factor of 0.45 which was obtained by relating the line-of-sight magnetic field measurements between the two instruments using pixel-by-pixel comparison (Riley et al. 2014). The temporal evolution of MAI averaged over 189 patches termed as Mean Magnetic Activity Index (MMAI), is shown in Figure 2.5 (upper panel) and clearly depicts the solar cycle variation.

In addition to MAI, we also use 10.7 cm radio flux ($F_{10.7}$)[2] which is a measurement of the integrated emissions at a wavelength of 10.7 cm over the entire solar-disk (Covington 1969; Ermolli et al. 2014) and is expressed in solar flux units ($1\,\mathrm{sfu} = 10^{-22}\,\mathrm{Wm^{-2}\,Hz^{-1}}$). The $F_{10.7}$ values are interpolated to the same temporal grid to have the same length as the mode parameters. The radio flux data is acquired using two fully automated radio telescopes from the Dominion Radio Astrophysical Observatory (DRAO) in Kaleden, British Columbia. Due to the Sun and Earth having a variable distance between them, the flux values are corrected to account for this annual variability. DRAO measures $F_{10.7}$ three times a day, and records their data virtually online on the government of Canada's space weather website. The temporal variation of $F_{10.7}$ is plotted in the lower panel of Figure 2.5 showing the solar cycle variation similar to MMAI.

Finally, mode parameters are compared to sunspot number, which is yet another measurement of solar activity. As solar activity increases, sunspot count increases as well, leading to sunspot count and MMAI having a direct correlation, which is useful to keep in mind when comparing mode parameters to these quantities separately. It should be noted that the data values for radio flux and sunspot count were not calculated personally, but rather pulled from public data bases (radio flux[3] and sunspot count[4] respectively). For the MMAI, the GONG and MDI magnetograms were converted to daily MAI values and then provided along with the mode parameters at the start of this research.

[2] https://www.spaceweather.gc.ca/forecast-prevision/solar-solaire/solarflux/sx-5-en.php

[3] https://www.spaceweather.gc.ca/forecast-prevision/solar-solaire/solarflux/sx-5-en.php

[4] https://www.sidc.be/SILSO/datafiles

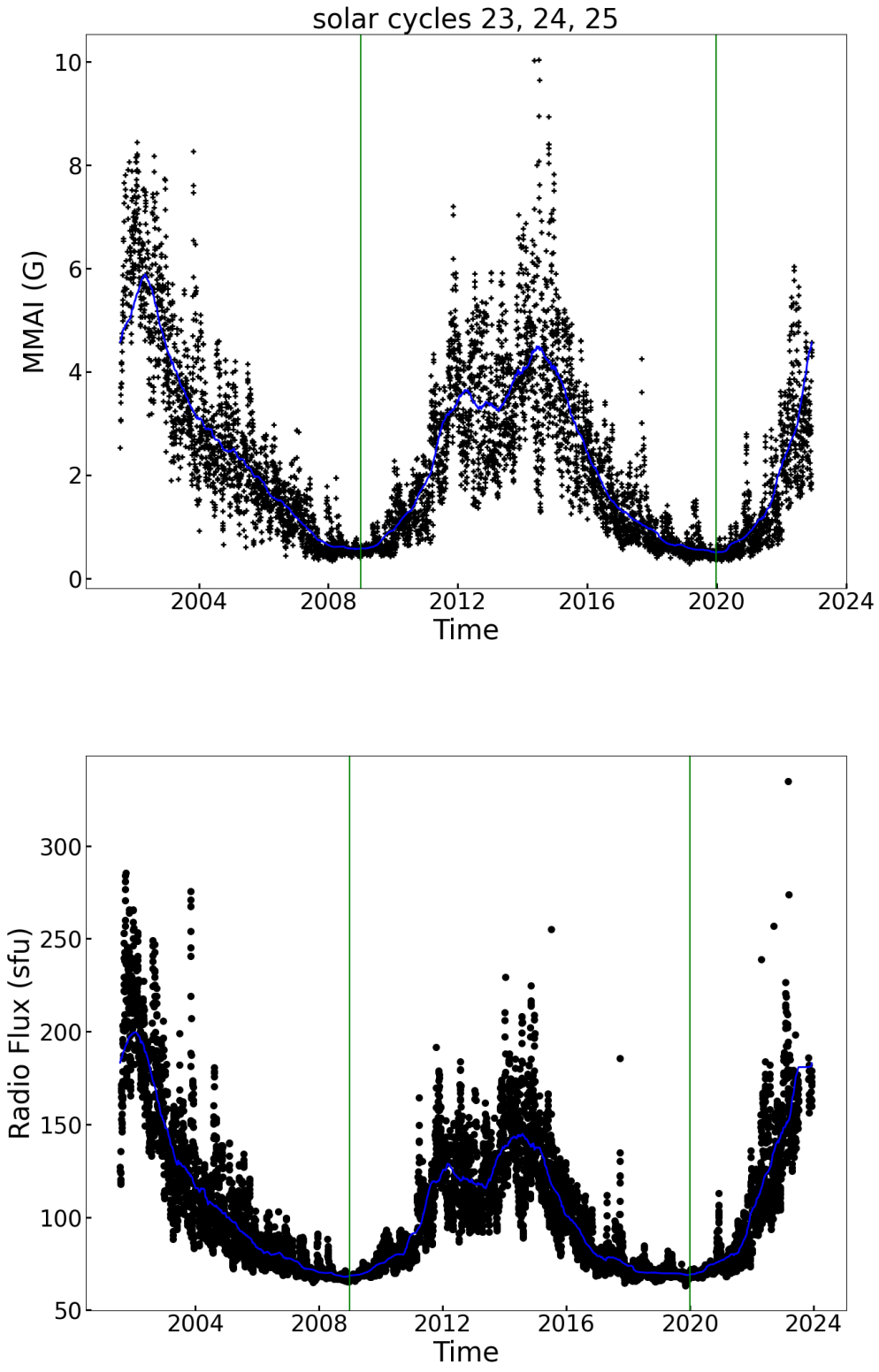

FIGURE 2.5: Temporal variation of mean magnetic activity index (upper panel) and 10.7 cm radio flux (bottom panel). Blue lines represent the smoothed values, where the smoothing is performed by a boxcar average over one year. The green vertical lines mark the boundaries of different solar cycles.

CHAPTER 3: Analysis

3.1 Mode Parameters vs Frequency

The first step of analyzing the oscillation mode parameters used in this research was to check and verify the previously documented trends in various mode parameters. This was done through plotting various parameters either as a function of frequency or ℓ, as well as ℓ vs frequency, which is commonly known as an $\ell - \nu$ diagram. This sanity check was done on the mode parameters derived from the disk center patch of the data for 2001.

In the graph of ℓ vs frequency (Figure 3.1), we can see that there are seven distinct "lines" where our data points for modes of oscillation fall. This corresponds to the different n wave numbers that the modes have, with the bottom line being f modes or surface modes, with an n value of zero. Other lines represent p_1 through p_6 modes. These distinct lines also appear in the plot of amplitude vs frequency, with the leftmost line being $n = 0$. Furthermore, each point on the lines represent different ℓ values, producing a series of points that have unique n and ℓ values as expected of modes with different resonance frequencies. The amplitude vs frequency graph is shown to have largest errors in high ℓ corresponding to each n. This is due to the fact that at high ℓ values, the modes blend together and have a lower signal to noise ratio which introduces large errors during the fitting procedure. Comparing these plots with those from Howe et al. (2004), we observe similar trends, and thus we were confident that our analysis is on the correct track.

3.2 Mean Value Calculation

With our sanity check complete, we move on to further analyzing our data to see how mode parameters vary in relation to solar activity, applying different constraints on the data such as timescale of averaging. For the analysis we first

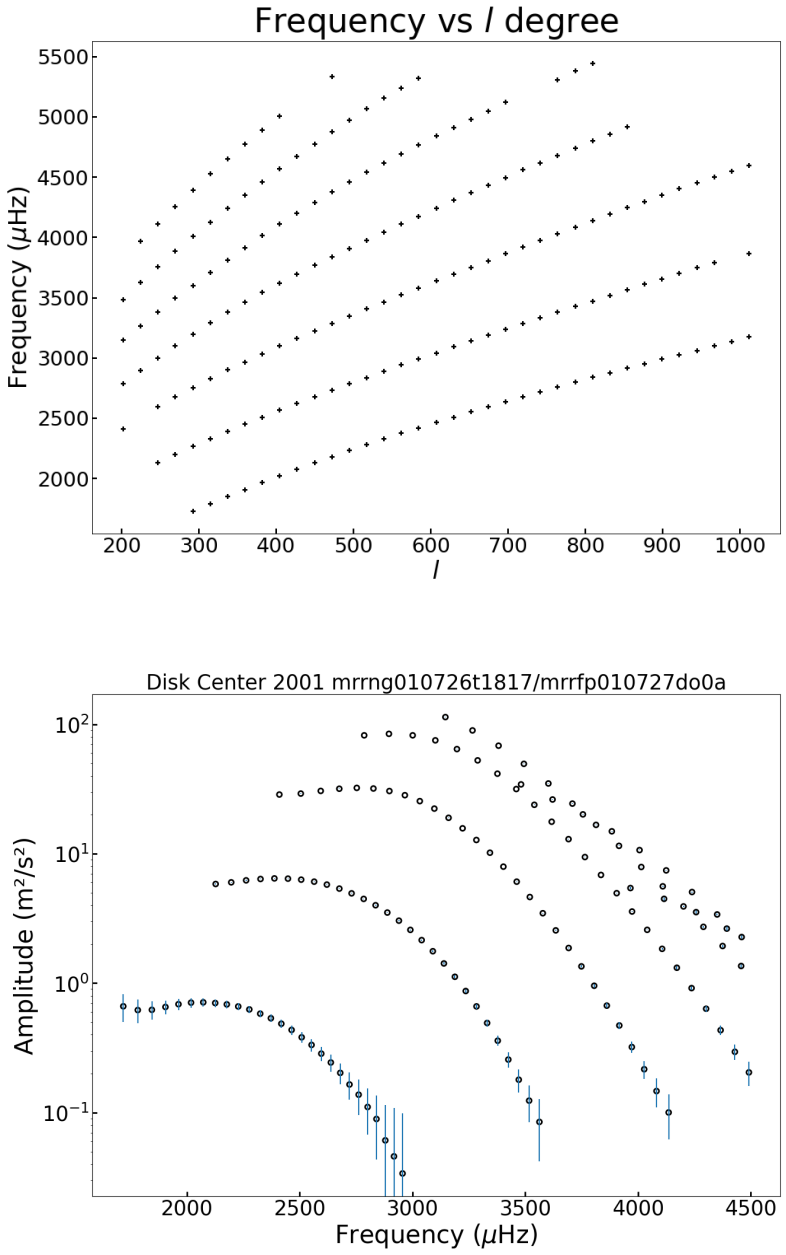

FIGURE 3.1: Top: The frequency, ν, vs degree, ℓ, for each mode from the disk center patch on a single ring-day in July 2001. Here the bottom line is the surface modes (n=0) with the higher lines being higher n level modes. Bottom: The amplitude vs frequency for the same day. Note the addition of error for amplitude values, as well as amplitude being represented in log rather than linear space.

converted the raw parameter values into "fractional values" by subtracting a reference value. The reference period was chosen during the minimum of solar activity,

here the period of 2007-2008 was used. A period of solar minimum is chosen as that period is marked by low magnetic activity between solar cycles 23 and 24 and therefore the oscillation modes will be least influenced by magnetic activity during these times, making their parameter values closest to what could be considered as the values corresponding to the quiet period of a solar cycle. We average parameters from this period, so that we are left with a single averaged mode parameter for each n and ℓ mode. Now when we calculate correlations between mode parameters with solar activity, rather than correlating the raw values we subtract the mean values from the respective raw values, giving us the difference or "δ" of the raw value from the minimum period value. Furthermore we divide this δ value by the parameter values from the minimum period, thus creating fractional δ values to correlate rather than raw data values. This method is similar to that used in Howe et al. (2004). Thus, negative fractional values are values smaller than the mean values from solar minimum, and likewise values larger than solar minimum will be positive fractions.

With our fractional values calculated, we can now analyze them with different cadences and observe their correlation with solar activity. First we calculate values to find how the mode parameters change on a daily basis, where instead of creating our fractional values with the reference values from solar minimum, we find the mean parameter values for each mode from the 189 patches. To find the correlation with solar activity, we first chose three different oscillation modes with the data only from 2001 and use MMAI as the measure of solar activity (Figure 3.2). These three modes have different n and ℓ values, meaning that they have different frequencies. Modes of different frequencies, and therefore also of different ℓ carry information about different depths of the Sun (Table 3.1). This is due to low ℓ degree modes typically going deeper into the Sun than higher degree modes (Demarque & Guenther 1999).

After these three modes were individually correlated with solar activity, a further investigation of different frequency ranges and how their parameters correlate with MMAI was carried out, with the frequency ranges being 1500-2500, 2500-3500, and 3500-4500 μHz respectively.

n	ℓ	ν (μHz)	Linear Correlation Coefficient	
			Amplitude	Mode Width
2	450	3030.0	-0.72	0.71
5	584	5236.0	0.57	-0.11
6	382	4890.0	0.29	0.27

TABLE 3.1: Pearson's linear correlation coefficients between mode amplitude and mode width with MMAI for three different modes from data of 2001 (Figure 3.2).

In a different analysis, we isolated the data corresponding to individual solar cycles 23, 24 and 25 bases on the sunspot counts, so that we could study how the correlations change over different solar cycles. We took this portion of the data analysis further by analyzing two more mode parameters beyond amplitude and damping rate, and we calculated and measured mode energy and energy supply rate for each of the three solar cycles. Mode energy is a measurement of how much energy an oscillation mode has, while energy supply rate is how the energy of the mode changes over time. These parameters are derived with the simple calculation of energy being the amplitude multiplied by mode width ($A \times \Gamma$) and supply rate being amplitude times the squared mode width ($A \times \Gamma^2$).

We next sought to understand how the correlation between mode parameters and solar activity changed with respect to solar hemisphere. We do this by neglecting any patch in the Sun with a latitude of 0 degrees, meaning any patch on the solar equator was not considered to be in either the northern or southern hemisphere. After applying this constraint to our data we are able to correlate mode parameters with MMAI as well as hemispheric sunspot count, observing how different hemispheres of the Sun could have separate levels of correlation with solar activity, and if a the modes of a particular hemisphere were shifted more or less by activity.

The final analysis we seek to place on our data is to analyze our temporal fractional values in the same cadence as used in the analysis of global modes which are obtained from the full disk and not localized regions. Global helioseismology typically averages their data in periods of three GONG months, which translates to 108 days. Averaging the fractional values this way allowed us to compare our results with those from global modes to understand the anomalous temporal variations seen in the mode amplitude described in the next chapter.

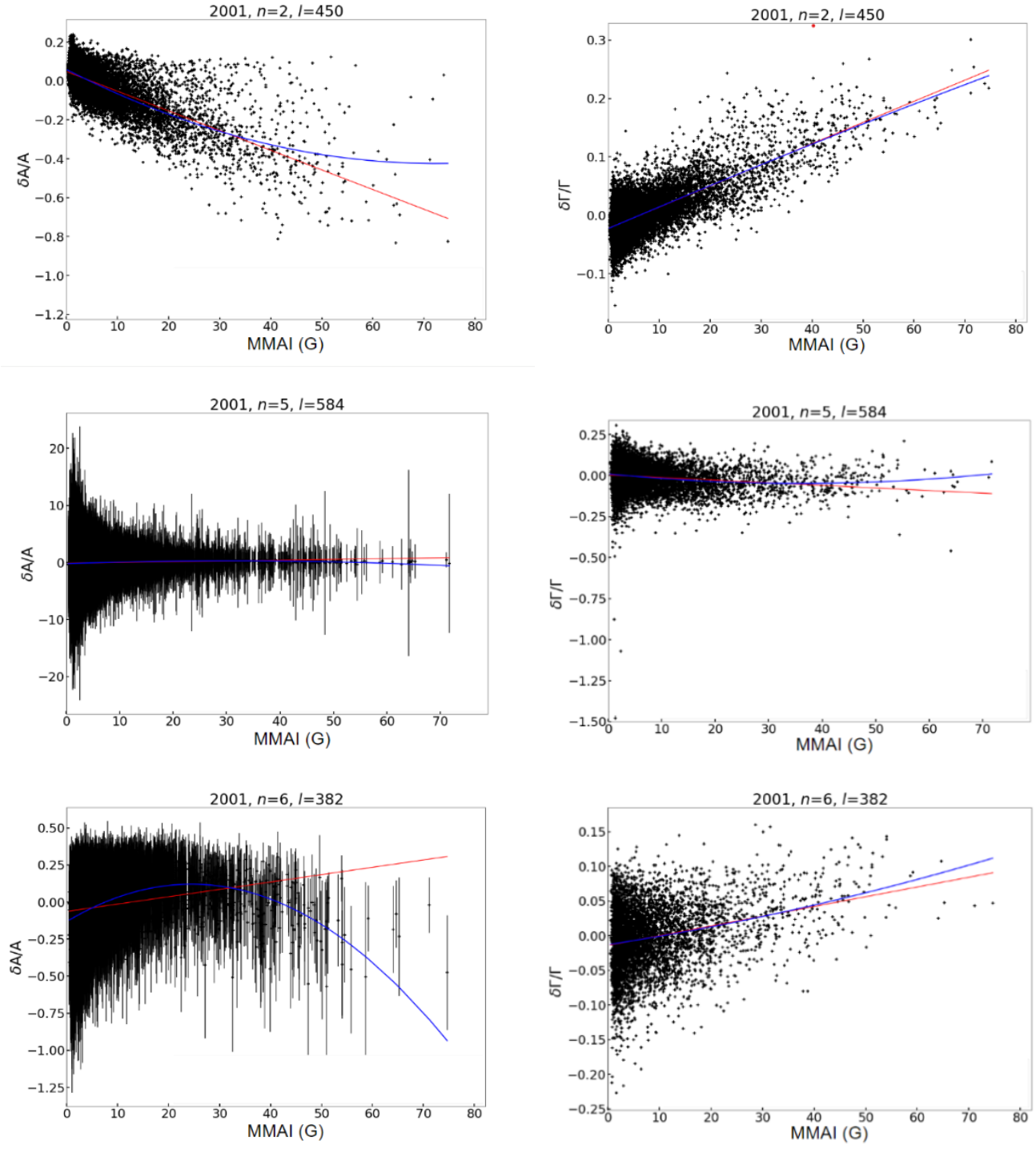

FIGURE 3.2: Fractional value of amplitudes (left panels) and mode widths (right panels) for three different oscillation modes from 2001 are shown as a function of mean magnetic field. The red and blue lines shows the resuls of linear and quadratic fits, respectively. The n and ℓ values are mentioned on the top of each panel.

CHAPTER 4: Results

Figure 4.1 shows the distribution of mode amplitude (top panel) and mode widths (bottom panel) as a function of frequency where these parameters are averaged over a single ring-day during the minimum (black dots) and maximum (red dots) periods (2008 and 2014 respectively) of solar activity. It is evident that for a period of low solar activity (2008) the mode amplitude values are less than the period of high solar activity (2014). The opposite can be said of the damping of the modes, or the mode width, which has greater values during the period of high solar activity. Thus, the mode widths are in phase with solar activity level, while the amplitudes are in anti-phase with activity; i.e. a positive correlation for mode widths and negative correlation for amplitudes. As mentioned earlier, we have extended the analysis to cover the distribution of mode energy and mode energy supply rate in Figure 4.1. It is evident that both these quantities decrease during the solar maximum as compared to the minimum period indicating anti-correlation with solar activity.

In order to understand how the mode parameters change on a daily basis, we computed the fractional changes in mode amplitudes and widths for each patch by subtracting the daily mean from each mode and then averaging the fractional values over all modes. Similarly, we averaged the MAI value of 189 patches to obtain the mean magnetic activity index (MMAI) over the same day. Figure 3.2 shows the fractional shifts of amplitude and mode width as a function of MMAI for different n and ℓ values during 2001 ($n = 2$ and $\ell = 450$ frequency approximately 3030 μHz, $n = 5$ and $\ell = 584$ frequency approximately 5326 μHz, and $n = 6$ and $\ell = 382$ frequency approximately 4890 μHz). It should be noted that different n and ℓ values correspond to different frequencies and hence carry information from different depths.

We find that the amplitudes show different trends with magnetic field depending on the frequency; the lowest frequency indicates a decrease with activity while at the two higher frequencies the amplitude shows slight enhancement with solar activity. Observing mode widths, we find that the highest frequency mode width decreases very slightly with activity, while the lower two frequency modes have

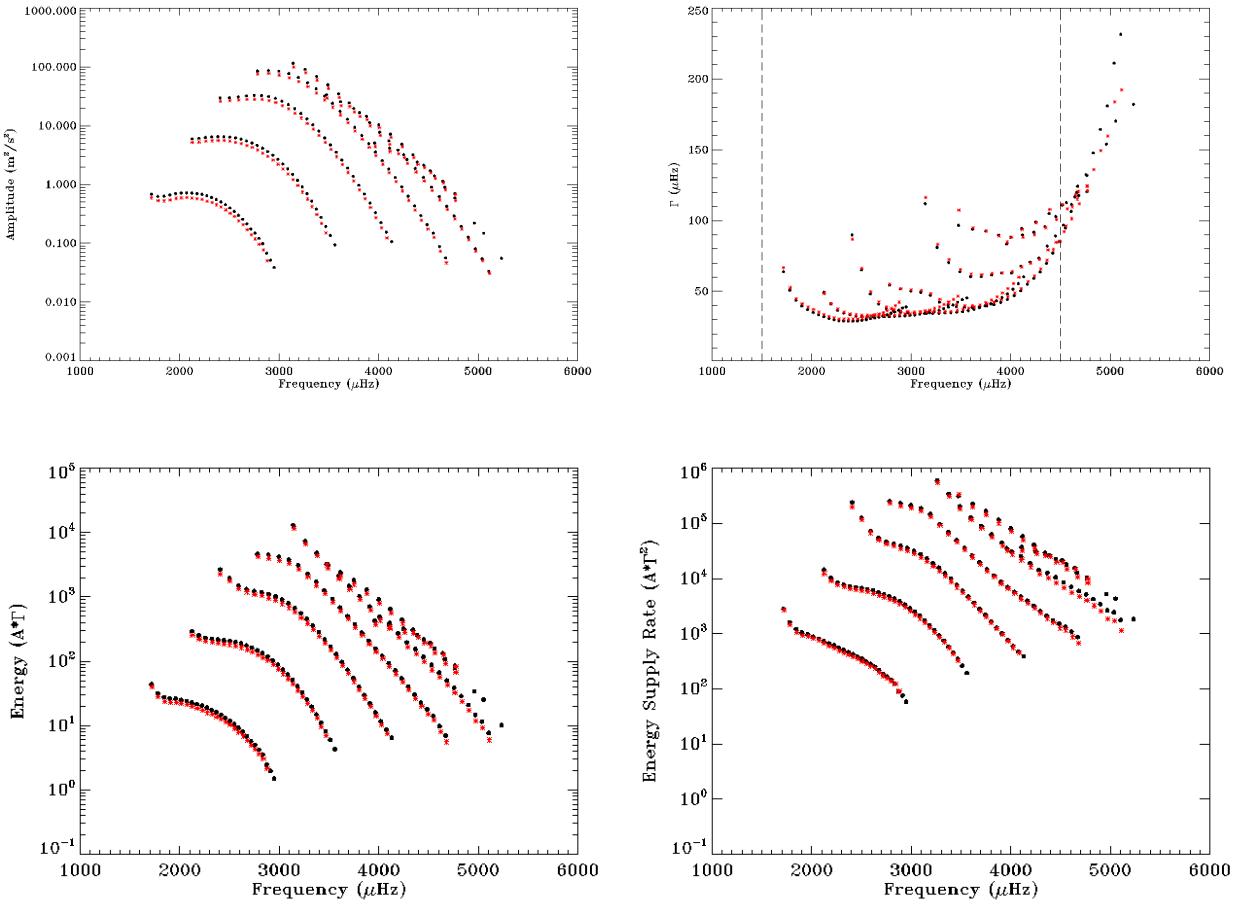

FIGURE 4.1: Mode amplitude (top left) and mode width (top right) as a function of frequency during a low activity period in 2008 (black) and high a activity period in 2014 (red). Mode energy (bottom left) and mode energy supply rate (bottom right) as a function of frequency during a low activity period in 2008 (black) and high a activity period in 2014 (red). This clearly demonstrates that these mode parameters vary with the level of magnetic activity, as the values are shifted for each parameter at high solar activity.

their mode width increase with activity. The Pearson's linear correlation values for amplitude and mode widths are given in Table 3.1. Thus observing these distinct n and ℓ values allows us to observe how the trend between mode parameters and magnetic activity could change with depth. For the remainder of the results, we have restricted the analysis to a frequency range of 1500-4500 μHz.

After computing our daily fractional values, they are then correlated with the MMAI and linear Pearson's correlation coefficients are computed. Figure 4.2 shows the coefficients as a function of MMAI, color coded for different solar cycles. We

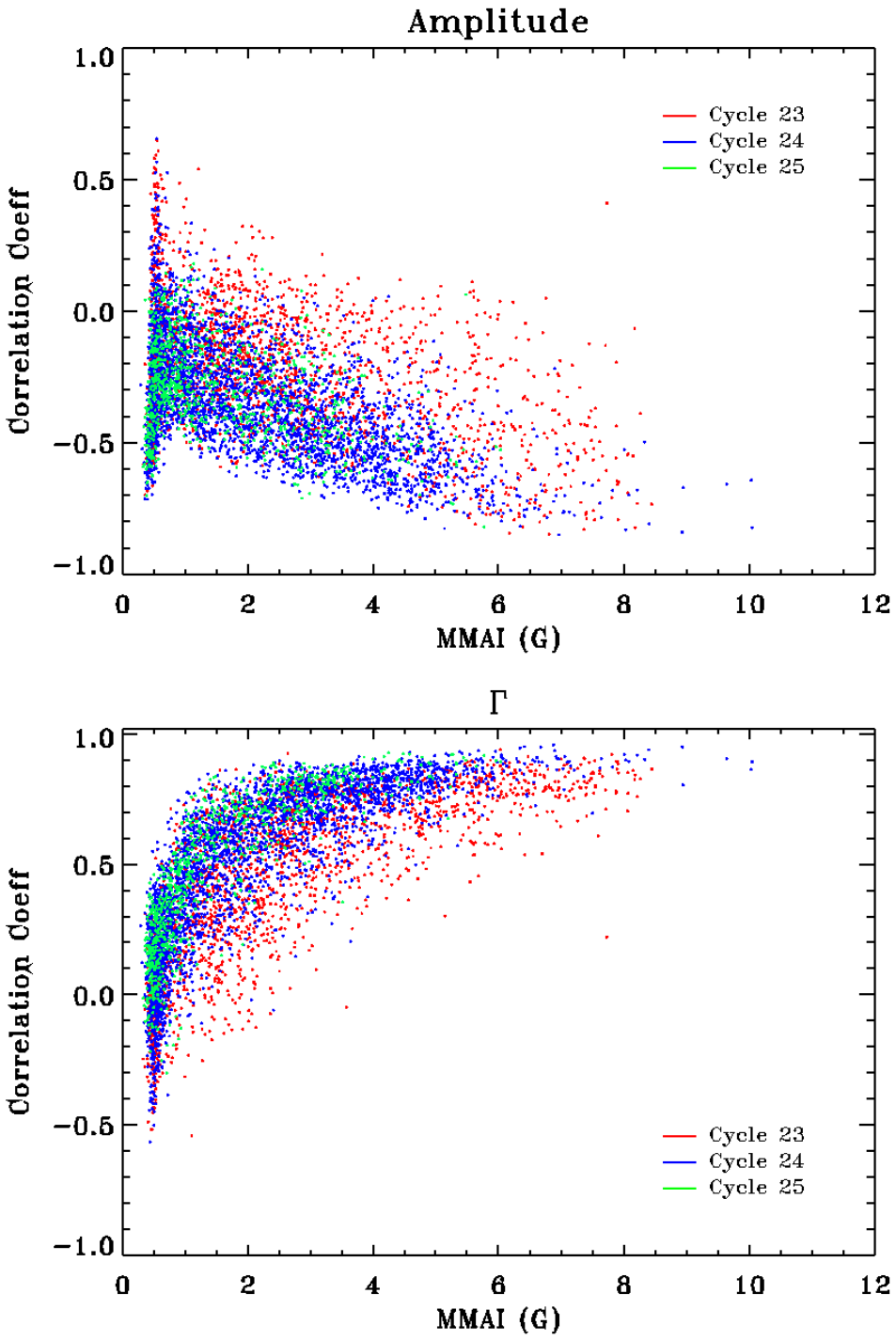

FIGURE 4.2: Linear correlation coefficients between MMAI and mode amplitude (top), and between MMAI and mode width (bottom). Different solar cycles are color coded as shown on the graph. The difference in the position of the correlations demonstrate how mode parameter correlation changes for each solar cycle.

do a similar plot of coefficients as a function of radio flux in Figure 4.5. It is evident that for all cycles, the amplitude decreases with MMAI (negative correlation between mode excitation and MMAI). This means that with increasing solar activity, peak power of oscillation modes decreases. Observing mode width, we can see that it has an overall increase with MMAI (positive correlation between mode width and MMAI). This provides evidence that as magnetic activity increases we see an increase in the damping rate of acoustic oscillation modes. Another thing to note is that since damping rate is inversely proportional to the lifetime of a mode, the lifetime of acoustic modes decreases as activity increases. We also note anti-correlation for the line widths (and positive correlations for amplitude) at lower MMAI values but these are not significant. Similar anti-correlation was also noted in mode frequencies at lower MMAI values in (Tripathy et al. 2015). An explanation for this is that the MMAI of the Sun has to be relatively strong in order for the correlation between mode parameters to be seen, and thus when MMAI is weak during the minimum period, the fractional values are too small to provide meaningful correlation.

The temporal variation of the correlation coefficients are depicted in Figure 4.3. The solid line in the figure indicates the coefficient where the coefficients that were using a boxcar average over a period of one year. These trend lines clearly illustrates how different solar cycles have different correlation coefficients, although the overall negative or positive value of the correlations remains the same in each cycle for amplitude and mode width. One can also observe a nearly 1 year periodicity in the correlation coefficients, illustrated especially well in solar cycle 23 for amplitude. This is probably be due to the effect of the B_0 angle which is the angle between the Earth and the Sun's disk center location as viewed from the Earth and changes throughout the year.

In order to comprehend the cyclic variations of the mode parameters, we have calculated the fractional values over all time period where the reference value taken over the minimum activity period of 2007-2008. We take the reference values from a minimum period as this will provide parameters shifted the least by solar activity, and thus are as close to the natural values of the mode parameters as possible. The fractional variation of amplitudes and mode widths (red lines) as a function of time is shown in Figure 4.4 where we only plot the trend lines which

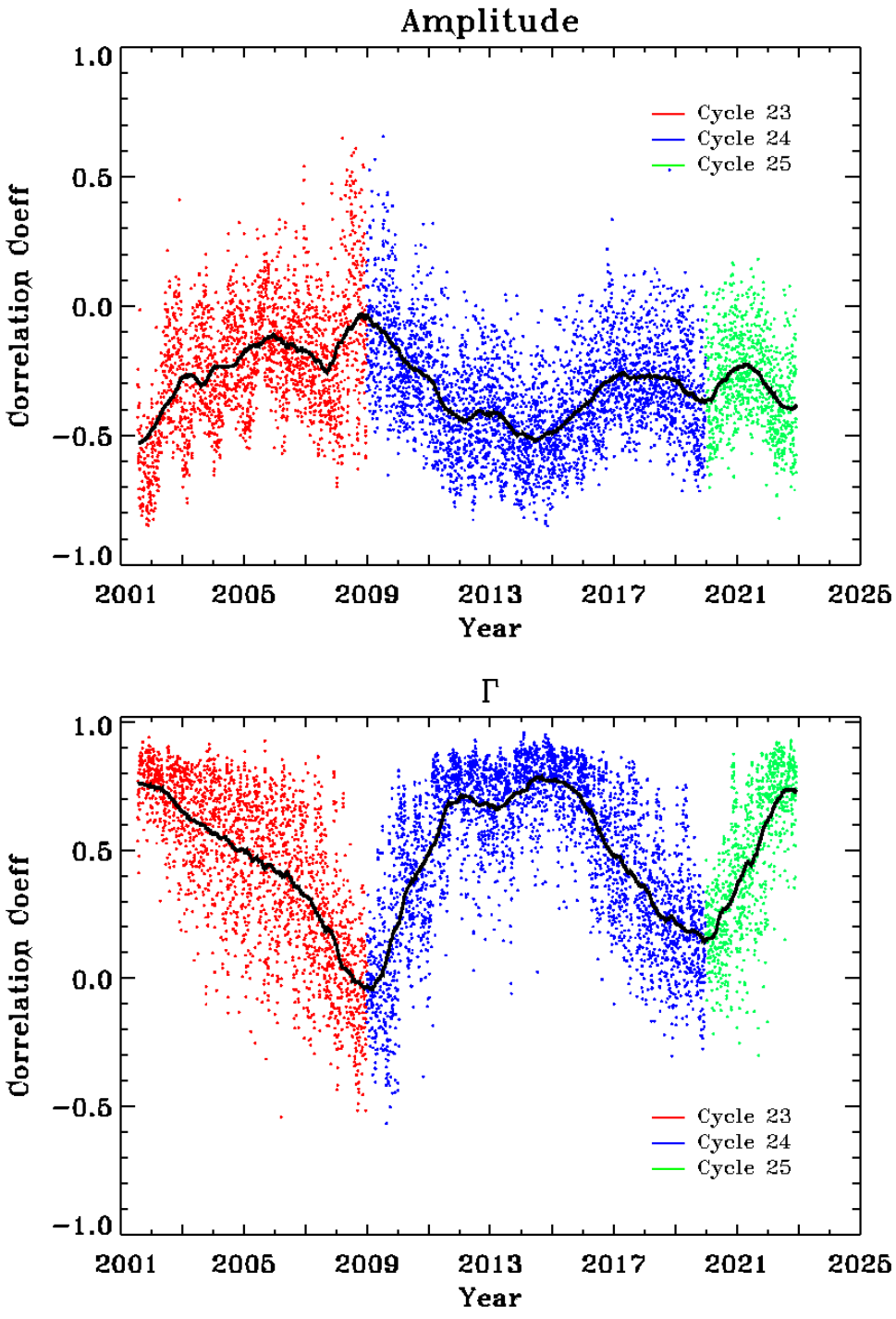

FIGURE 4.3: Linear correlation coefficients between radio flux and mode amplitude (top), and between radio flux and mode width (bottom) as a function of time. The magnitude of correlation goes to zero around 2008. This is due to that period of time being a period of solar minimum, so there is barely any magnetic activity to correlate with.

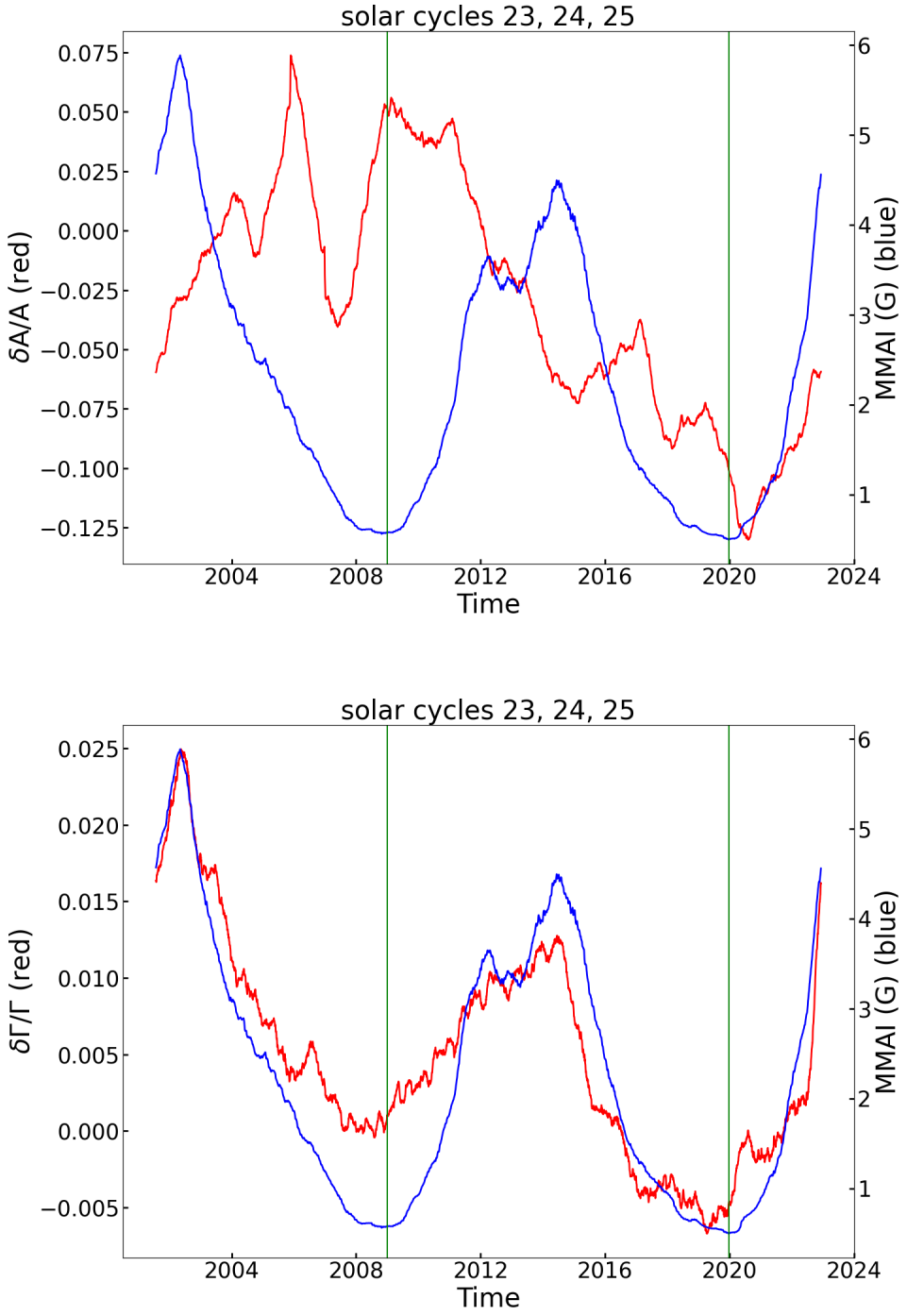

FIGURE 4.4: Temporal variation in mode amplitude (top) and mode width (bottom) for all data. The red lines show the trend lines for each parameter which are boxcar averaged over one year. The blue lines in each panel is the boxcar average of MMAI. The mode width lines up well with the trends of magnetic activity, showcasing its good in phase correlation with MMAI. One can observe the areas where amplitude does not have an anti correlation with MMAI, namely the anomalous periods around 2008, 2018, and the ascending phase of solar cycle 25.

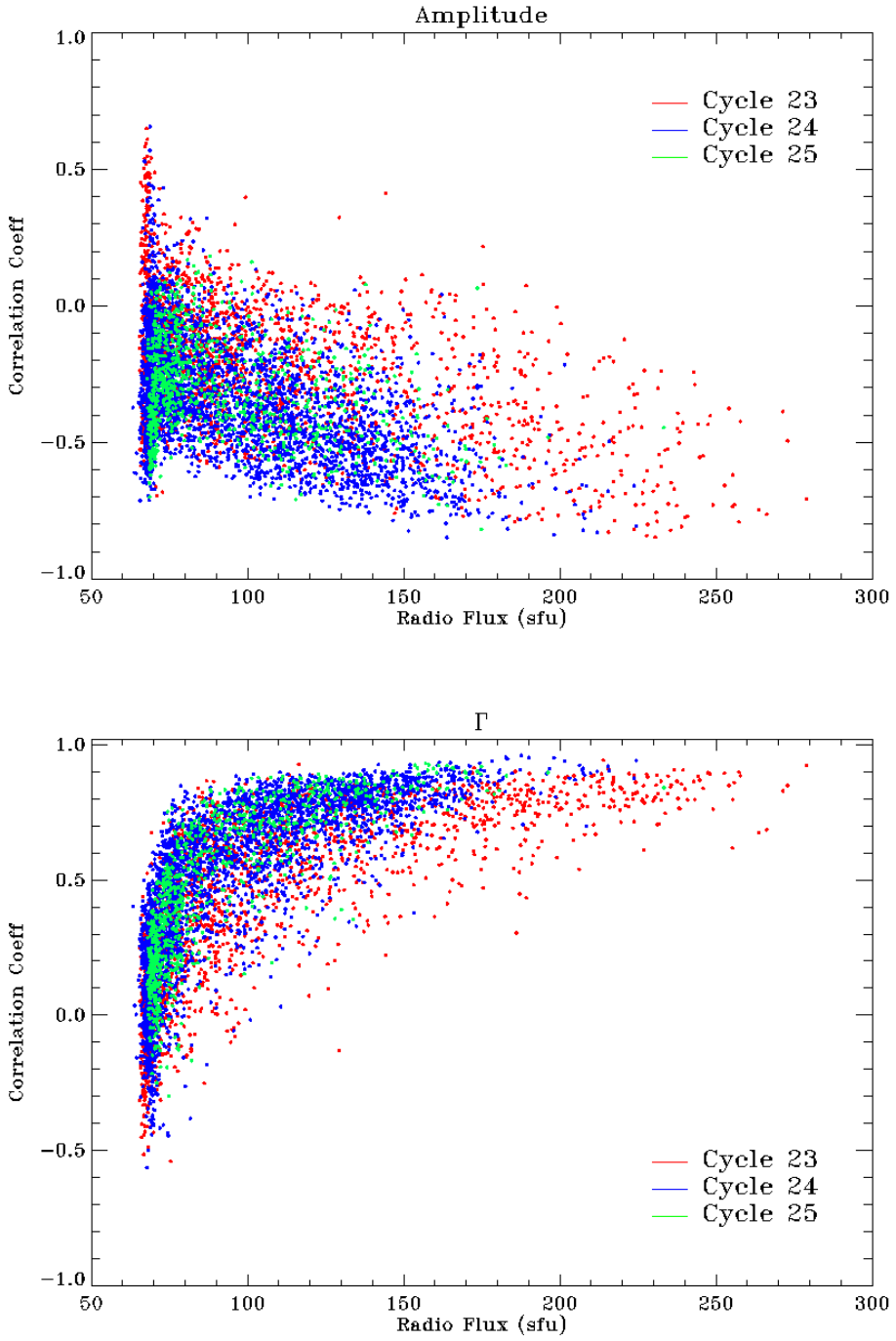

FIGURE 4.5: Linear correlation coefficients between radio flux and mode amplitude (top), and between radio flux and mode width (bottom). Different solar cycles are color coded as shown on the graph. The difference in the position of the correlations demonstrate how mode parameter correlation changes for each solar cycle.

are the boxcar average values over a period of one year. The figure also shows the boxcar avearged MMAI values (blue curve). It is evident that the trends for amplitude and mode width are similar to what was seen in Figure 4.3 where the mode width is in phase with MMAI, while amplitude is in anti-phase with MMAI. These relations are similar to previous findings (Broomhall et al. 2015; Kiefer et al. 2018).

There are, however, a few anomalous periods where the amplitude is in phase with MMAI especially during the minimum period of cycle 23 and 24 and ascending phase of cycle 25. The effect could be instrumental in origin or a processing problem during the merging of Dopplergrams from the six GONG sites. It is also plausible that the background power is significantly changed during these periods although the study of Tripathy et al. (2006) found that the background amplitude is uncorrelated with the solar activity. But we note that this investigation was carried out using the global oscillation data prior to the extended minimum period of cycle 24. However, analyzing global data during 1996-2018, Kiefer et al. (2018) found jumps in global amplitude values during 2001 and 2005 epochs. The first jump was attributed to change in GONG cameras while the cause of the second jump was not found. The authors modeled the jumps by increasing the amplitude values as a function of ℓ and ν. The corrected amplitude values were then found to be anti-correlated with solar activity. However, there are significant differences between the data used in this study and that of Kiefer et al. (2018). While Kiefer et al. (2018) used global modes in the ℓ range of 0-150 computed from time series of 108 days in an interval of 36 days, we use high-degree modes in the ℓ range of 180-1300 computed over an interval of 1664 minutes.

We wanted to pursue a similar approach to model the amplitude jumps seen in our analysis, but this could not be carried out due to the limited time. However, to compare the results between the two studies, we computed the mode amplitudes and widths over the interval of 108 days and analyzed their temporal variations. This is described later in this chapter.

We also performed linear and quadratic fits between the the mode parameters and MMAI (Figure 4.6) for different solar cycles. The values are given in Table 4.1. It can be seen seen that the fitting coefficients change for each solar cycle. This

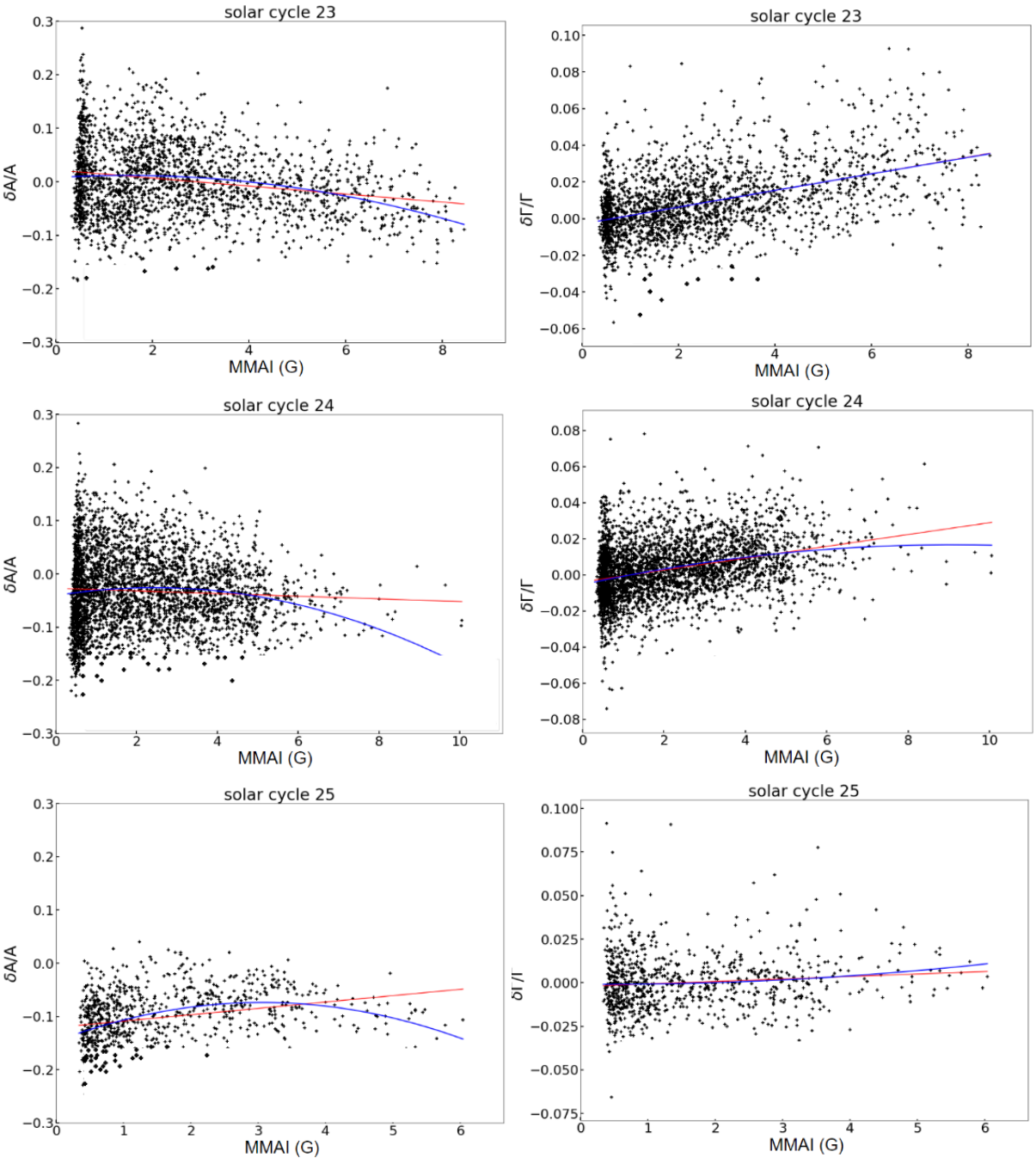

FIGURE 4.6: Temporal variation in mode amplitude (left) and mode width (right) for individual solar cycles 23, 24, and 25. The red lines indicate the linear fits while the blue lines indicate the quadratic fit. The values of these fit lines can be seen in Table 4.1. One can notice visually the differences in the parameters per cycle with how each parameter has a different red and blue line for every solar cycle.

solar Cycle	Parameter	Linear Fit	Quadratic Fit
23	Amplitude	$-7.47x+21.8$	$-1.88x^2+5.48x+7.84$
24	Amplitude	$-2.48x-2.70$	$-2.52x^2+12.3x-40.7$
25	Amplitude	$12.0x-121$	$-7.76x^2 + 47.5x-146$
All data	Amplitude	$-3.04*10^{-3}x-29.9$	$2.66x^2+16.5x-46.0$
23	Mode width	$4.55x-2.83$	$-1.03*10^{-3}x^2+4.62x-2.91$
24	Mode width	$3.28x-3.88*10^{-2}$	$-2.64*10^{-1}x^2+4.82x-5.32$
25	Mode width	$1.42x-2.09$	$3.65*10^{-1}x^2-2.58*10^{-1}x-0.88$
All data	Mode width	$3.89x-3.97$	$5.02*10^{-2}x^2+3.58x-3.66$

TABLE 4.1: The fitted parameters from linear and quadratic fits between mode amplitude and mode width with mean magnetic activity index (MMAI) for solar cycles 23, 24, and 25 and all data.

is because each solar cycle has a unique pattern and level of magnetic activity. Table 4.1 also includes the fitting coefficients when all 21 years of the data is analyzed. As expected this yields a resulting amplitude with a negative linear correlation with MMAI, and a mode width with a positive linear correlation with MMAI provide the correlation coefficients in the table. One of the anomalous periods for the amplitude can be seen with these fits, as the linear fit for the ascending phase of solar cycle 25 has a positive linear coefficient, as opposed to the expected negative coefficient seen in solar cycles 23 and 24.

Since the relation between mode parameters and activity proxies differs for different n and ℓ values, we further analyze the temporal evolution of these parameters in three different frequency ranges (1500-2500, 2500-3500, and 3500-4500 μHz). The temporal variation of the mode parameters (red lines) for these ranges along with MMAI (blue lines) are shown in Figure 4.7. This once again demonstrates that oscillation modes from different depths have different levels of correlation with MMAI, as the fractional values for both amplitude and mode width change for each of the frequency ranges. It is still evident even with frequency range constraints that mode width holds a direct correlation with MMAI, while amplitude is anti correlated except for anomalous periods discussed earlier.

Figure 4.8 shows the temporal evolution of other two mode parameters we investigated: energy and energy supply rate. When correlated with magnetic activity,

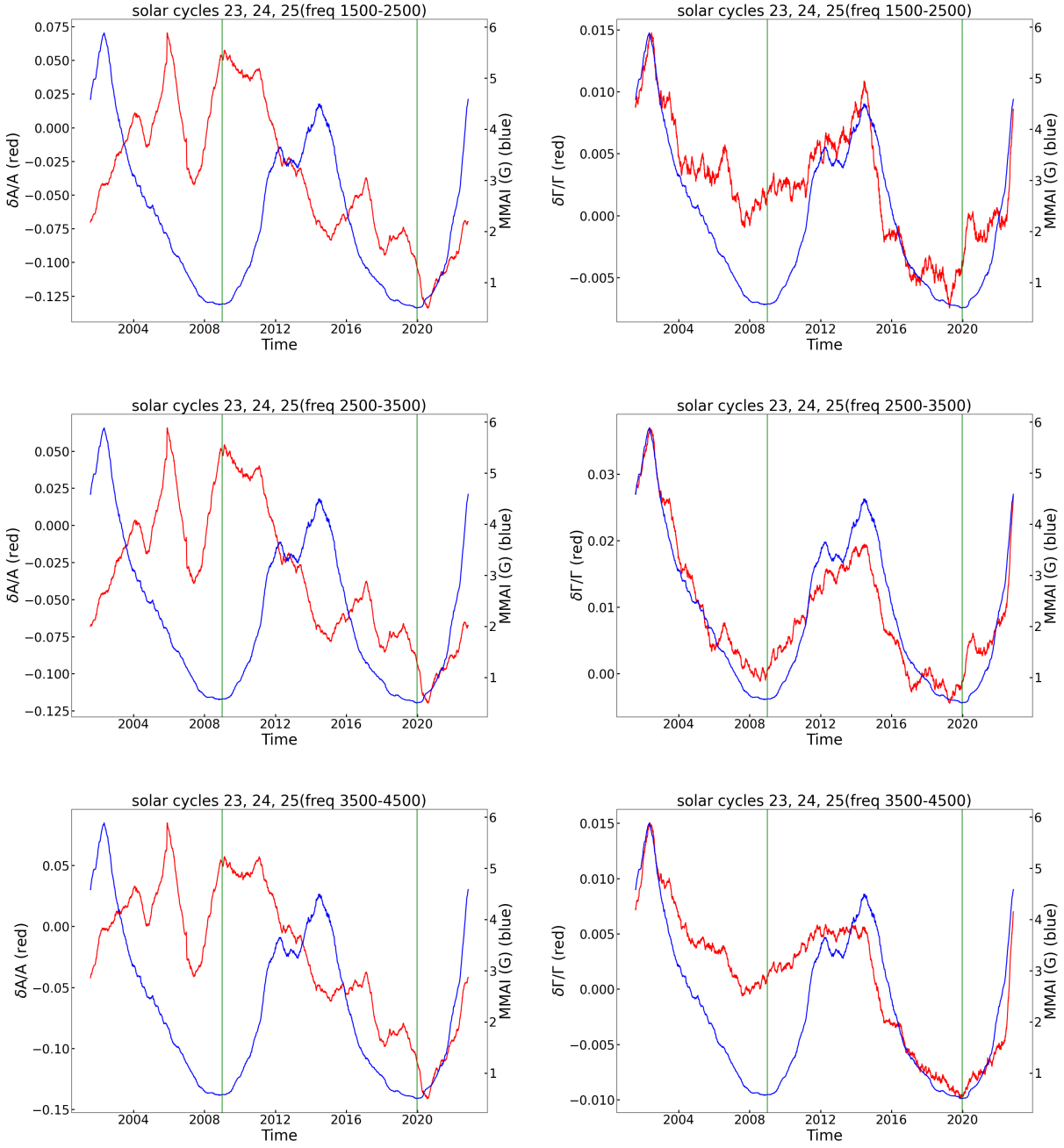

FIGURE 4.7: The red lines show the mode amplitudes (left panels) and mode widths (right panels) as a function of time for different frequency ranges. Only the trend lines which are boxcar averaged over one year are shown. The blue lines in each panel is the boxcar average of MMAI.

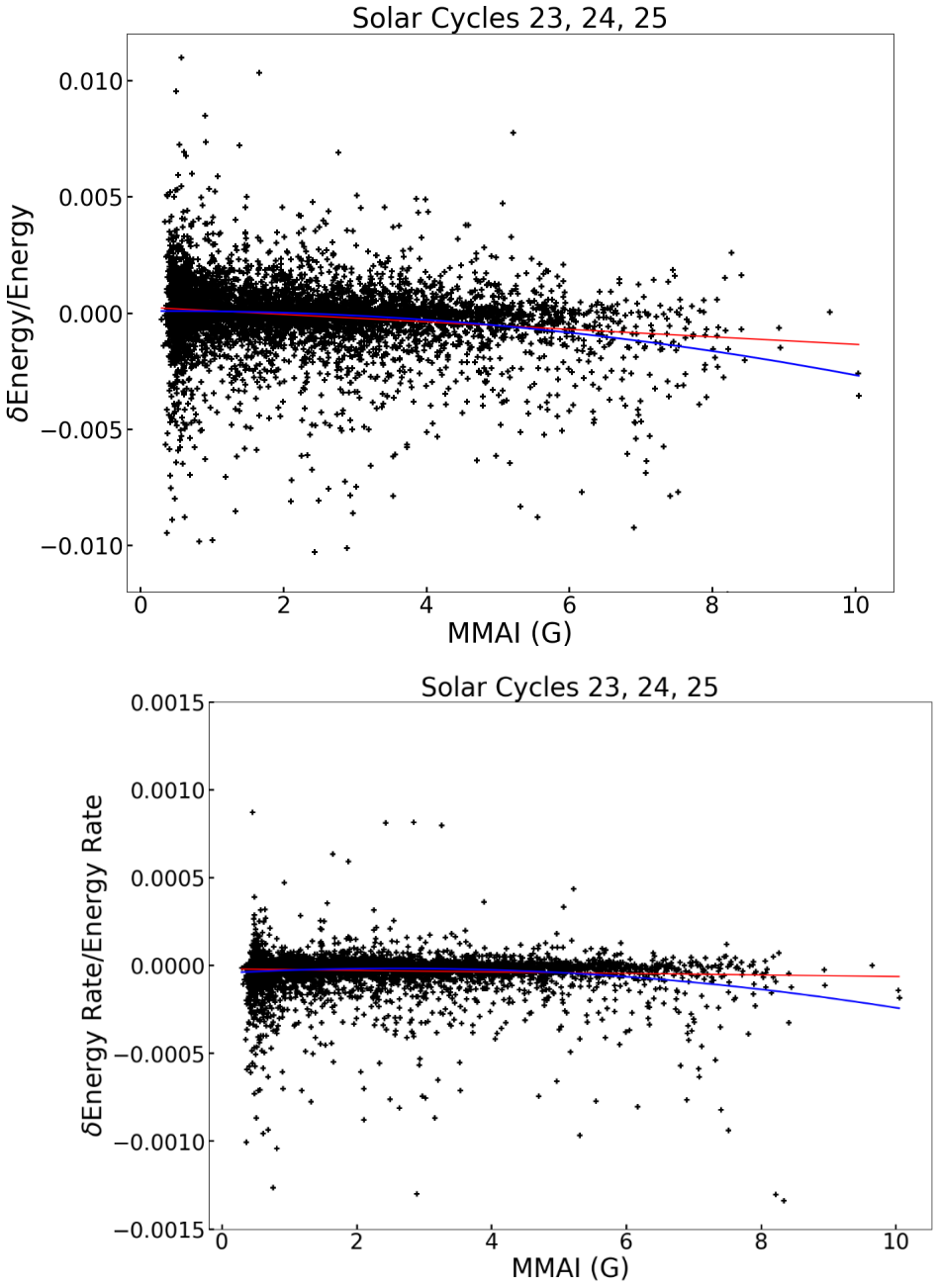

FIGURE 4.8: Temporal variation of mode energy (top) and energy supply rate (bottom) as a function of magnetic activity. The red lines indicate the linear fits while the blue lines indicate the quadratic fit.

Mode	Linear Correlation Coefficient			
Parameter	Cycle 23	Cycle 24	Cycle 25	All data
Amplitude	−0.30	−0.06	0.88	0.03
Mode width	0.81	0.68	0.30	0.73
Energy	−0.74	−0.84	−0.95	−0.75
Energy supply rate	−0.43	−0.29	0.36	−0.21

TABLE 4.2: The linear Pearson correlation coefficients between the four parameters under study and MMAI for different solar cycles and all data. It is shown here that the linear correlation for each parameter changes per solar cycle.

Mode	Linear Correlation Coefficient	
Parameter	Northern Hemisphere	Southern Hemisphere
Amplitude	0.12	−0.35
Mode width	0.07	0.40
Energy	−0.23	0.15
Energy supply rate	0.24	−0.18

TABLE 4.3: The linear Pearson correlation coefficients between the four parameters under study and MMAI for each solar hemisphere. The correlation in both hemispheres is much weaker than the correlations of the combined data.

both parameters seem to display negative correlations with solar activity (Table 4.2). We also analyzed these parameters independently for each solar cycle (Figure 4.9) and found that the correlation coefficients are different for each solar cycle, just like amplitude and mode width analyzed over entire period. Once again the anomalous behaviour of the mode amplitudes can be seen in the linear fit of energy supply rate of for cycle 25. We seek to further investigate why the energy supply rate for this cycle deviates from the expected behavior.

Since solar activity is known to be asymmetric between the northern and southern hemispheres, we have investigated the parameters separately for these two hemispheres. Figure 4.10 shows the same four parameters as a function of MMAI for the northern hemisphere, while Figure 4.11 shows the same parameters for the southern hemisphere. As before, the red lines indicate the linear fits while the blue lines indicate the quadratic fit. We also for the hemispheric data use daily number of sunspots as a metric of solar activity, and plot our four parameters as a function of sunspot count for the northern (Figure 4.12) and southern (Figure 4.13) hemispheres.

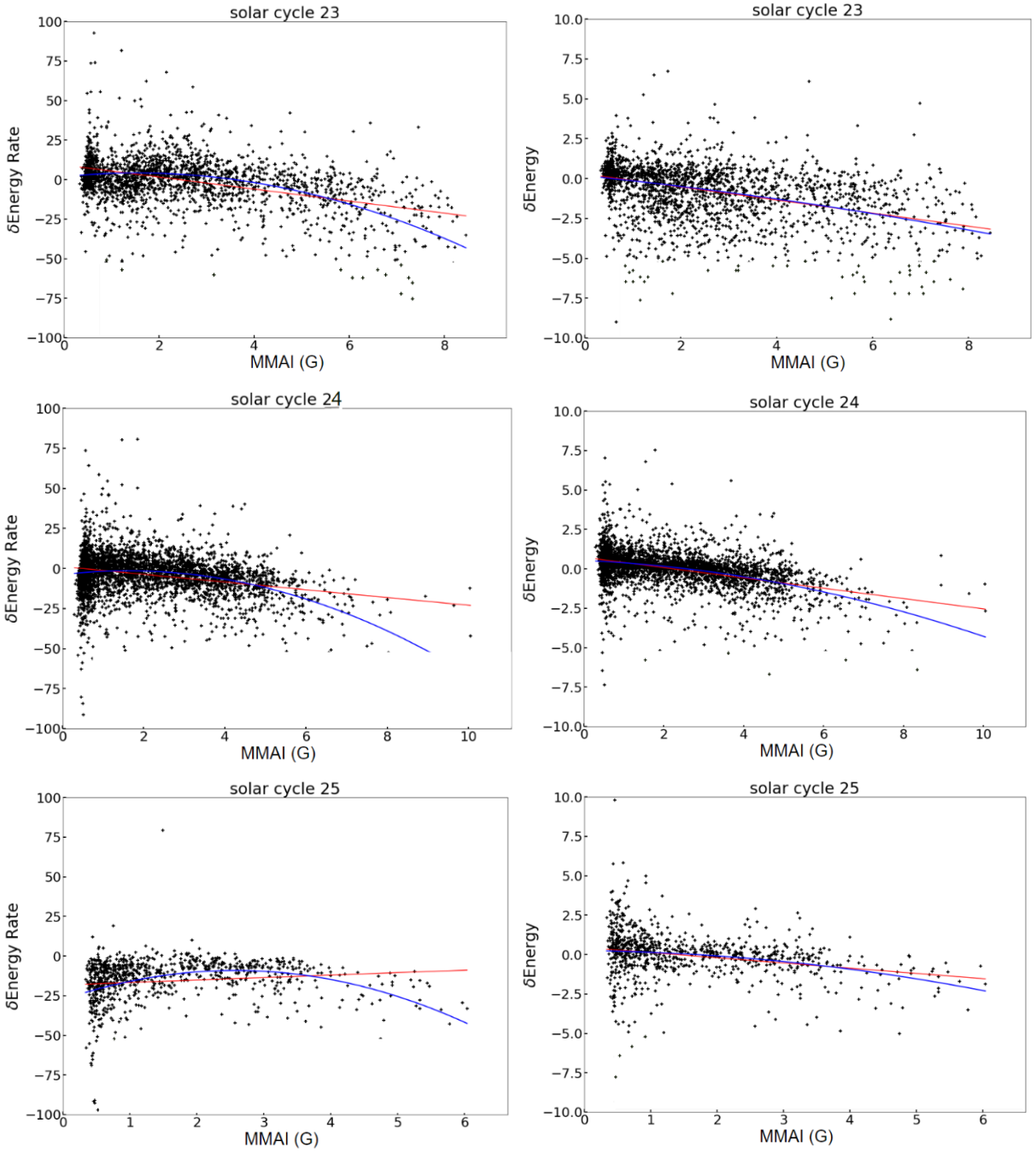

FIGURE 4.9: Temporal variation in mode energy supply rate (left) and mode energy (right) for solar cycles 23, 24, and 25. The red lines indicate the linear fits while the blue lines indicate the quadratic fit.

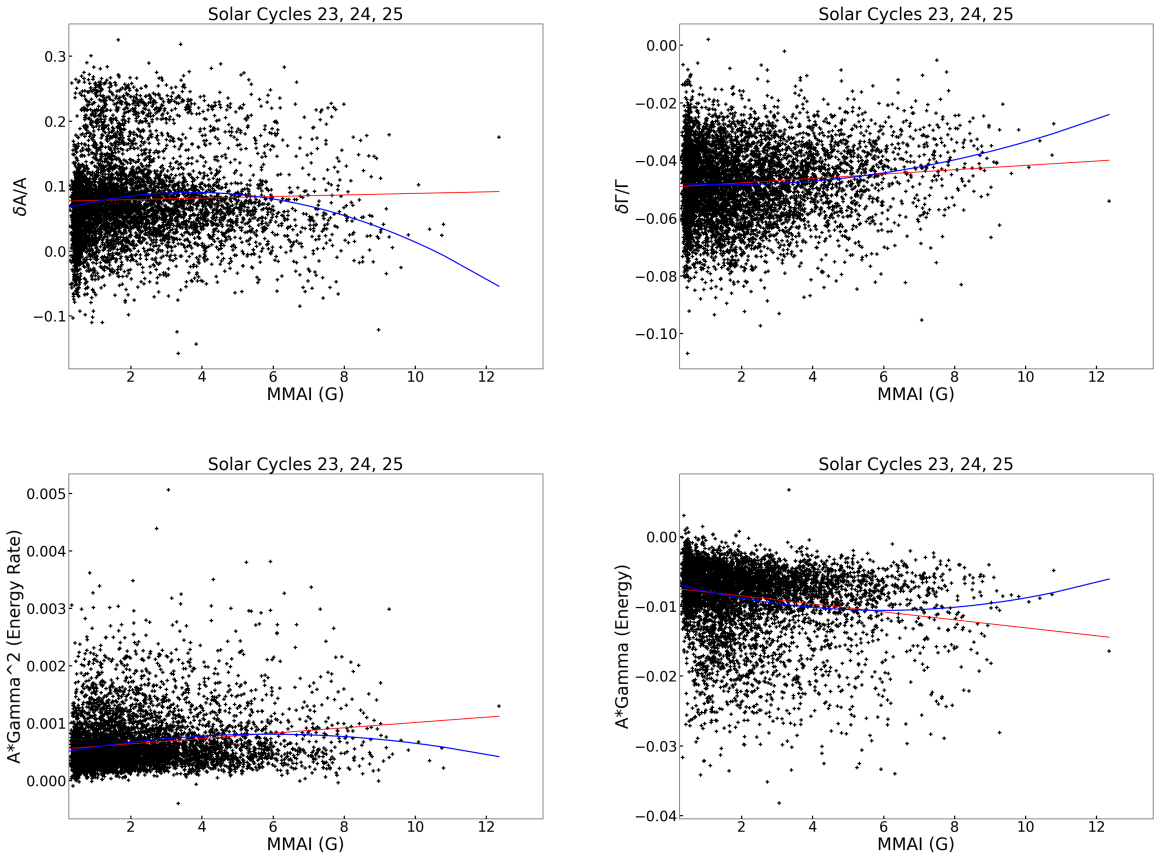

FIGURE 4.10: Mode Parameters vs MMAI for the northern hemisphere. The red lines indicate the linear fits while the blue lines indicate the quadratic fit. Just as with amplitude and mode width, one can notice visually the different fit lines for each solar cycle.

The most important and surprising result here is that all of the parameters in both hemispheres have significantly smaller correlation (or anti-correlation) coefficients with MMAI (Table 4.3). Notably amplitude and mode width can be seen to have much smaller linear anti correlation and correlation values for both hemispheres. The correlations for both of these parameters is larger in the southern hemisphere indicating stronger activity as compared to the northern hemisphere. It will be interesting to analyze phase-wise variations in the two hemispheres since the solar activity is known to be varying between hemisphere as a function of phase of the cycle.

As mentioned earlier, we wanted to compare our results with those from global mode analysis. In this context, we have computed the fractional parameters after

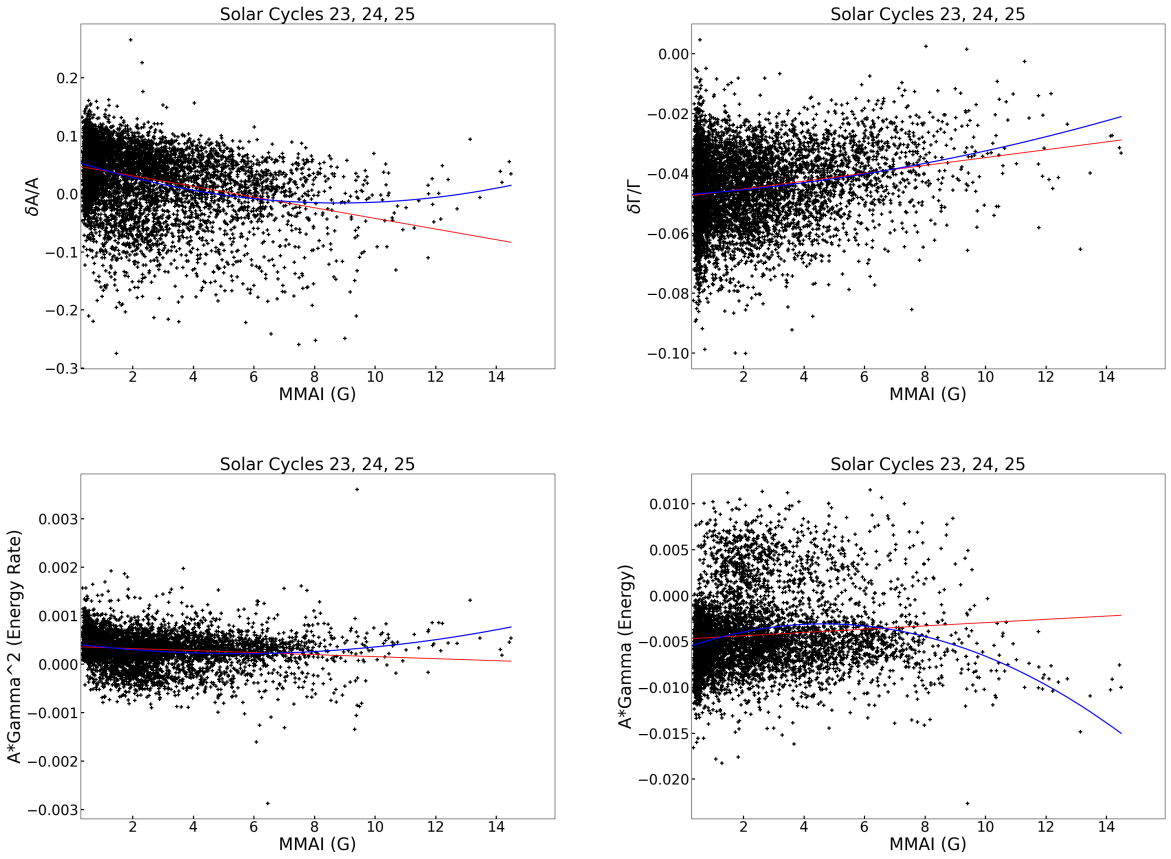

FIGURE 4.11: Mode Parameters vs MMAI for the southern hemisphere. The red lines indicate the linear fits while the blue lines indicate the quadratic fit.

averaging the mode parameters over the same 108 days corresponding to three GONG months. The resultant boxcar averaged mode amplitudes and widths and magnetic activity are shown in Figures 4.14 and 4.15, respectively. The trends in the data match the correlation and anti-correlation patterns that mode width and amplitude have in the non-108 day averaged data. This result is reassuring as it means the trends these two parameters experience are not changed by period of averaging. Thus it is reassuring that we can model the anomalous behavior seen in mode amplitudes (and energy and energy supply rates) to correct the values.

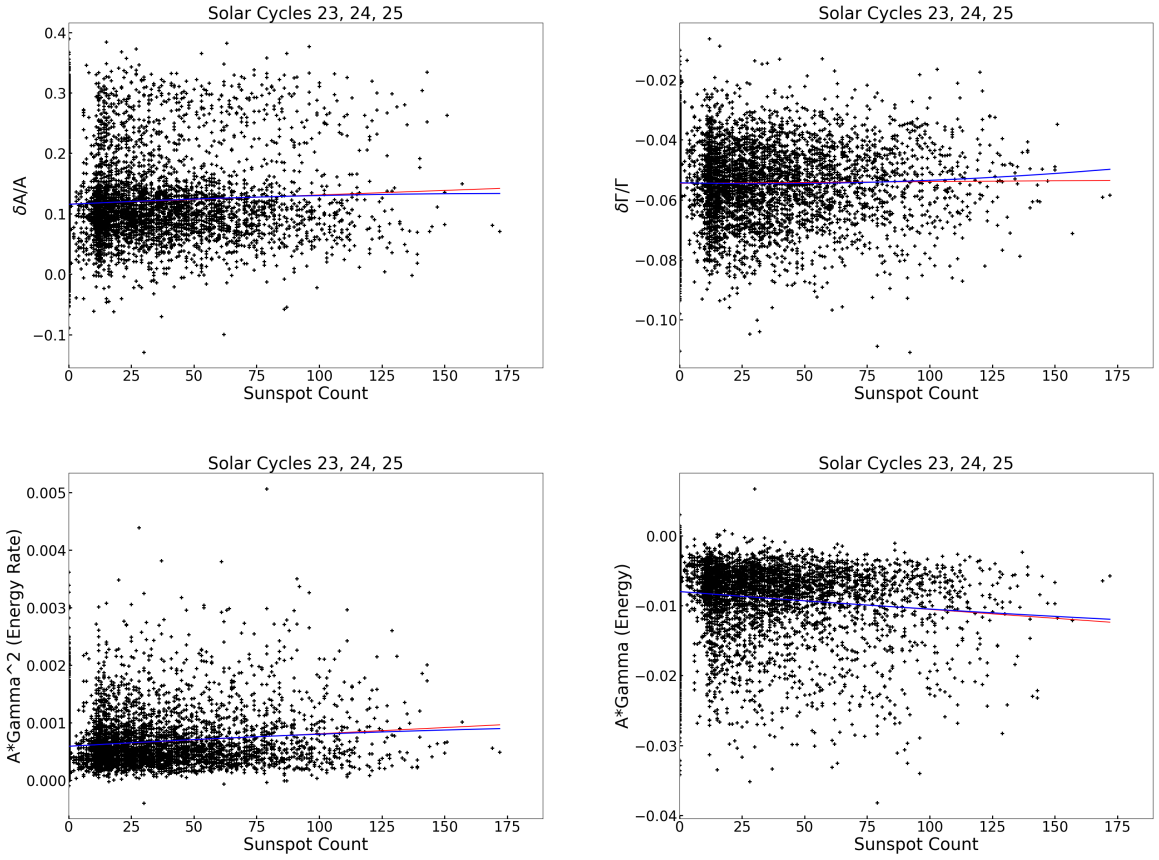

FIGURE 4.12: Mode Parameters vs number of sunspots for the northern hemisphere. The red lines indicate the linear fits while the blue lines indicate the quadratic fit.

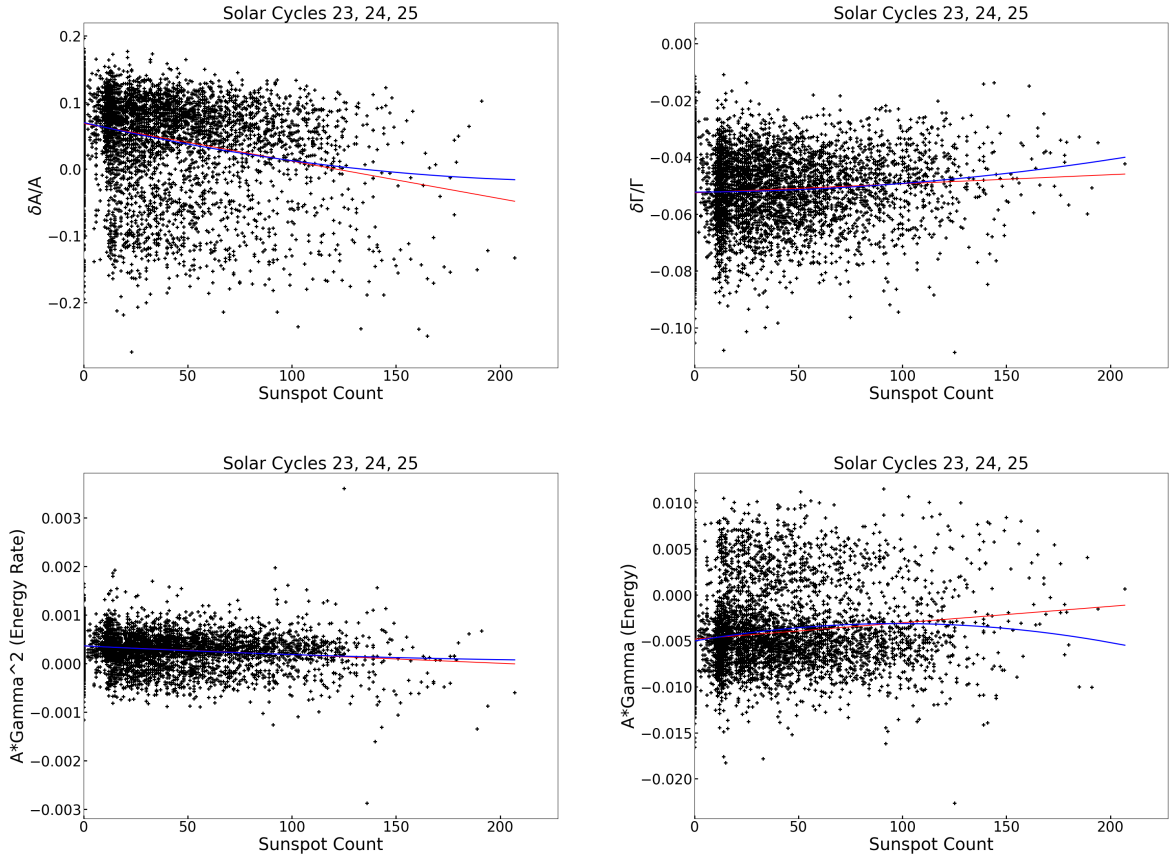

FIGURE 4.13: Mode Parameters vs number of sunspots for the southern hemisphere. The red lines indicate the linear fits while the blue lines indicate the quadratic fit.

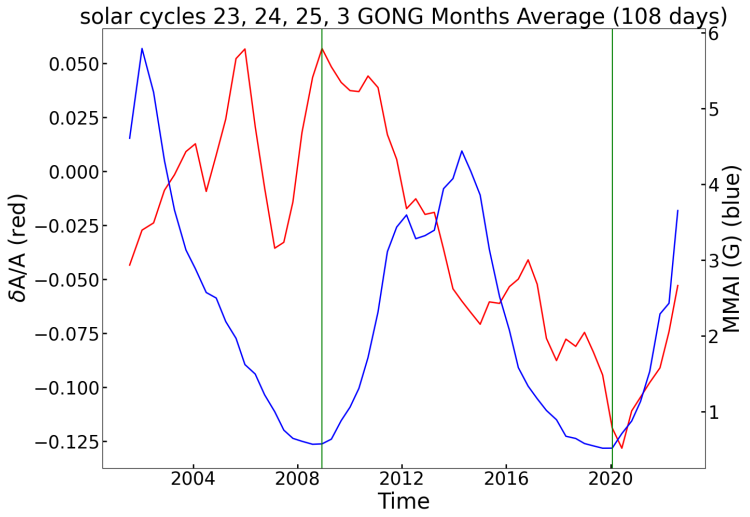

FIGURE 4.14: Temporal variation of mode amplitude and magnetic activity averaged over 108 days. This is the cadence over which global helioseismology parameters are computed.

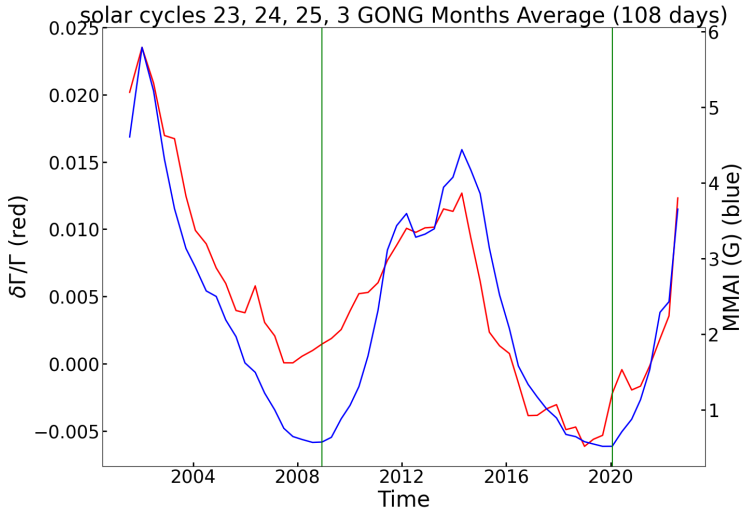

FIGURE 4.15: Temporal evolution of mode width and magnetic activity averaged over 108 days. This is the cadence over which global helioseismology parameters are computed.

CHAPTER 5: Conclusion

The purpose of this research was to analyze the parameters of acoustic modes of the Sun to understand how they change with respect to solar activity and solar cycles. We considered oscillation modes from solar cycles 23, 24, and 25 in order to understand how parameters of acoustic modes change by solar cycle. We also constrained the parameters based off of things like hemisphere and frequency range, in order to gain an understanding of how correlations with solar activity vary based off of things like hemisphere and depth of where the mode is generated.

We first process our data by taking the Dopplergrams made by GONG and perform a 3D-FFT on the data to extract the parameter values of the modes. Once this is complete, we perform a geometric and instrumental correction on the parameters. We then create fractional values to better interpret the results. We then correlate the mode parameters with various measures of solar activity. The measures of solar activity we use are MMAI, $F_{10.7}$ cm radio flux, and daily number of sunspots.

We find that the mode amplitude, energy and energy supply rate, which are measures of mode excitation, are in anti-phase with magnetic activity, while damping rate (mode width) is found to be in phase with activity. The correlation coefficients and linear and quadratic fits are also found to vary between different solar cycles since no two cycles have the same activity level. Our investigation also showed that different mode frequencies have different trends with respect to magnetic activity, which is suggestive of a depth dependence. We plan to investigate these different frequency ranges further, in an attempt to quantify the depth dependence. We also analyzed the behavior of the mode parameters in the northern and southern hemispheres separately and found that the correlation decreases significantly compared to the whole Sun. Finally, we compared our data that has been averaged in the same 108 days cadence as global helioseismology and concluded that it is plausible to model the anomalous behavior of the mode amplitudes in a way similar to those carried out in global modes. With this study, we have extended previously published results on the temporal variation of solar p-mode parameters to cover multiple solar cycles.

Bibliography

Basu, S., Antia, H. M., & Bogart, R. S. 2004, ApJ, 610, 1157, doi: 10.1086/421843

Broomhall, A. M., Pugh, C. E., & Nakariakov, V. M. 2015, Advances in Space Research, 56, 2706, doi: 10.1016/j.asr.2015.04.018

Chaplin, W. J., Elsworth, Y., Isaak, G. R., Miller, B. A., & New, R. 2004, MNRAS, 352, 1102, doi: 10.1111/j.1365-2966.2004.07998.x

Corbard, T., Toner, C., Hill, F., et al. 2003, in ESA Special Publication, Vol. 517, GONG+ 2002. Local and Global Helioseismology: the Present and Future, ed. H. Sawaya-Lacoste, 255–258

Covington, A. E. 1969, JRASC, 63, 125

Demarque, P., & Guenther, D. B. 1999, Proceedings of the National Academy of Sciences, 96, 5356, doi: 10.1073/pnas.96.10.5356

Elsworth, Y., Howe, R., Isaak, G. R., et al. 1993, MNRAS, 265, 888, doi: 10.1093/mnras/265.4.888

Ermolli, I., Shibasaki, K., Tlatov, A., & van Driel-Gesztelyi, L. 2014, Space Sci. Rev., 186, 105, doi: 10.1007/s11214-014-0089-8

Haber, D. A., Hindman, B. W., Toomre, J., et al. 2000, Sol. Phys., 192, 335, doi: 10.1023/A:1005235610132

Harvey, J., Tucker, R., & Britanik, L. 1998, in ESA Special Publication, Vol. 418, Structure and Dynamics of the Interior of the Sun and Sun-like Stars, ed. S. Korzennik, Noordwijk, 209

Harvey, J. W., Hill, F., Hubbard, R. P., et al. 1996, Science, 272, 1284, doi: 10.1126/science.272.5266.1284

Hill, F. 1988, ApJ, 333, 996, doi: 10.1086/166807

Hill, F., Bolding, J., Toner, C., et al. 2003, in ESA Special Publication, Vol. 517, GONG+ 2002. Local and Global Helioseismology: the Present and Future, ed. H. Sawaya-Lacoste, 295–298

Howe, R., Komm, R. W., Hill, F., Haber, D. A., & Hindman, B. W. 2004, ApJ, 608, 562, doi: 10.1086/392525

Jain, K., Tripathy, S. C., Basu, S., et al. 2013, in Astronomical Society of the Pacific Conference Series, Vol. 478, Fifty Years of Seismology of the Sun and Stars, ed. K. Jain, S. C. Tripathy, F. Hill, J. W. Leibacher, & A. A. Pevtsov, 193

Jain, K., Tripathy, S. C., Hill, F., & Pevtsov, A. A. 2021, PASP, 133, 105001, doi: 10.1088/1538-3873/ac24d5

Keith-Hardy, J. Z., Tripathy, S. C., & Jain, K. 2019, ApJ, 877, 148, doi: 10.3847/1538-4357/ab1b3b

Kiefer, R., & Broomhall, A.-M. 2021, MNRAS, 500, 3095, doi: 10.1093/mnras/staa3198

Kiefer, R., Komm, R., Hill, F., Broomhall, A.-M., & Roth, M. 2018, Sol. Phys., 293, 151, doi: 10.1007/s11207-018-1370-x

Komm, R. W., Howe, R., & Hill, F. 2000a, ApJ, 531, 1094, doi: 10.1086/308518

—. 2000b, ApJ, 543, 472, doi: 10.1086/317101

Leibacher, J. W., Noyes, R. W., Toomre, J., & Ulrich, R. K. 1985, Scientific American, 253. http://www.jstor.org/stable/24967776

Leighton, R. B., Noyes, R. W., & Simon, G. W. 1962, ApJ, 135, 474, doi: 10.1086/147285

Riley, P., Ben-Nun, M., Linker, J. A., et al. 2014, Sol. Phys., 289, 769, doi: 10.1007/s11207-013-0353-1

Snodgrass, H. B. 1984, Sol. Phys., 94, 13, doi: 10.1007/BF00154804

Tripathy, S. C., Hill, F., Jain, K., & Leibacher, J. W. 2006, in ESA Special Publication, Vol. 624, Proceedings of SOHO 18/GONG 2006/HELAS I, Beyond the spherical Sun, ed. K. Fletcher & M. Thompson, 93

Tripathy, S. C., Jain, K., & Hill, F. 2015, ApJ, 812, 20, doi: 10.1088/0004-637X/812/1/20